Geophysical Journal International

Geophys. J. Int. (2015) **201,** 1781–1800 doi: 10.1093/gji/ggv117
GJI Seismology

Seismoelectric beamforming imaging: a sensitivity analysis

P. El Khoury,[1] A. Revil[1,2] and P. Sava[1]

[1]*Department of Geophysics, Colorado School of Mines, Golden, CO* 80401*, USA. E-mail: arevil@mines.edu*
[2]*ISTerre, CNRS, UMR CNRS* 5275*, Université de Savoie, F-*73376 *cedex, Le Bourget du Lac, France*

Accepted 2015 March 9. Received 2015 February 21; in original form 2014 November 30

SUMMARY

The electrical current density generated by the propagation of a seismic wave at the interface characterized by a drop in electrical, hydraulic or mechanical properties produces an electrical field of electrokinetic nature. This field can be measured remotely with a signal-to-noise ratio depending on the background noise and signal attenuation. The seismoelectric beamforming approach is an emerging imaging technique based on scanning a porous material using appropriately delayed seismic sources. The idea is to focus the hydromechanical energy on a regular spatial grid and measure the converted electric field remotely at each focus time. This method can be used to image heterogeneities with a high definition and to provide structural information to classical geophysical methods. A numerical experiment is performed to investigate the resolution of the seismoelectric beamforming approach with respect to the main wavelength of the seismic waves. The 2-D model consists of a fictitious water-filled bucket in which a cylindrical sandstone core sample is set up vertically. The hydrophones/seismic sources are located on a 50-cm diameter circle in the bucket and the seismic energy is focused on the grid points in order to scan the medium and determine the geometry of the porous plug using the output electric potential image. We observe that the resolution of the method is given by a density of eight scanning points per wavelength. Additional numerical tests were also performed to see the impact of a wrong velocity model upon the seismoelectric map displaying the heterogeneities of the material.

Key words: Image processing; Electromagnetic theory; Magnetic and electrical properties; Hydrogeophysics.

1 INTRODUCTION

Electrokinetic phenomena are related to pore fluid motion relative to the skeleton of a porous material due to either electromagnetic or mechanical (seismic) disturbances (Hunter 1981; Pengra *et al.* 1999). In solvent-saturated porous materials (water-saturated, partially water-saturated or saturated by some oils behaving as solvents, see Revil & Jardani 2010), the seismoelectric (seismic-to-electric) coupling is associated with the partial conversion of mechanical energy of seismic waves into electromagnetic energy due to the presence of electric, hydraulic and/or mechanical discontinuities within the porous material (Pride & Haartsen 1996). In geophysics, the seismoelectric method consists of sending a seismic wave into the subsurface and recording the generated electromagnetic signals. Such signals include the interface response (also called seismoelectric conversion), that bear important information about the physical properties (porosity, permeability, and electrical conductivity) of the media (e.g. Pride & Haartsen 1996). In addition, as the seismic wave propagates through the porous material, an electric signal, called the coseismic effect, can be recorded by a network of electrodes when the seismic wave travels in between the electrodes (Frenkel 1944). This coseismic electric field is confined to the seismic wave, itself traveling with the seismic waves (e.g. Pride & Haartsen 1996). Since the first field observations made by Ivanov (1939), the seismoelectric method has been used to investigate a growing number of problems in exploration geophysics and near-surface geophysics including the exploration of glaciers (Kulessa *et al.* 2006), the water content in the vadose zone (Dupuis *et al.* 2007), sulphide deposits (Kepic *et al.* 1995), the monitoring of fracturing (Haas *et al.* 2013) just to cite a few.

In the 1990s, Pride & Haartsen (Pride 1994; Pride & Haartsen 1996; Haartsen & Pride 1997) developed a seismoelectric theory for water-saturated materials by coupling Biot's theory (Biot 1962a,b) and Maxwell's equations (Maxwell 1865) through a source current density of electrokinetic nature. Pride's theoretical modelling is based on three assumptions, (1) solving solid and fluid displacement vectors using Biot's theory, (2) solving the electromagnetic problem in the diffusive limit of Maxwell's equations and (3) using an electrokinetic theory based on the use of the zeta potential, a local electrostatic potential defined inside the electrical double layer coating the surface of the solid phase (e.g. Gouy 1910; Chapman 1913; Hunter 1981; Revil *et al.* 2013). For a typical 3-D model, the

© The Author 2015. Published by Oxford University Press on behalf of The Royal Astronomical Society.

Downloaded from http://gji.oxfordjournals.org/ at Colorado School of Mines on July 1, 2015

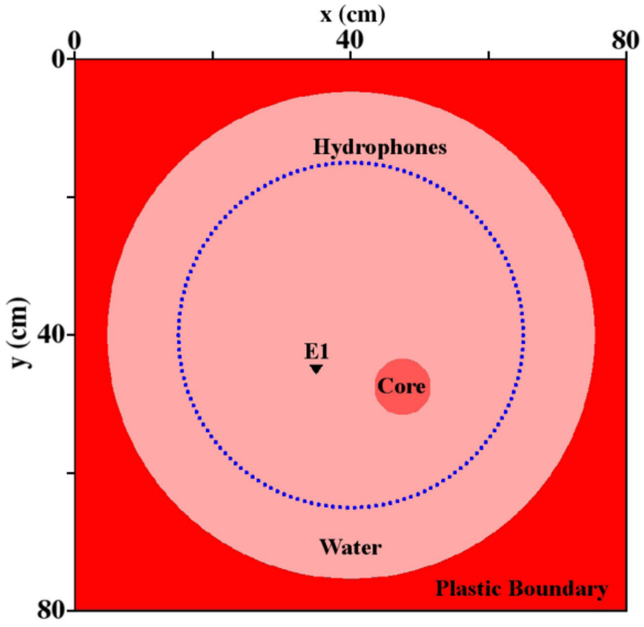

Figure 1. Schematic 2-D model representing an 80 cm × 80 cm tank with 7.5-cm-core submerged in a water medium surrounded by a plastic boundary. The triangle represents the location of electrode E1 while the reference electrode E2 is placed at infinity and the dark blue dots correspond to source–receiver hydrophones location (see Table 1 for the values of the material's properties).

number of unknowns in the partial differential equations governing the propagation of the seismic waves in a Biot-type medium is six: three components of the solid phase displacement vector and three for the fluid phase displacement vector. Once the seismic field has been computed, the electromagnetic fields are evaluated using the diffusive limit of the Maxwell equations accounting for inductive coupling between the electrical and magnetic fields. Several works have focused on producing some analytically based full-waveform modelling of the seimoelectric signals using Pride theory in layered materials considering fully coupled Maxwell's equations (Grobbe *et al.* 2012; Grobbe & Slob 2013; Smeulders *et al.* 2014).

Alternative formulations of the seismoelectric theory have also been developed by Revil, Jardani and co-workers (e.g. Jardani *et al.* 2010; Revil & Jardani 2010; Araji *et al.* 2012; Sava & Revil 2012; Revil & Mahardika 2013; Revil *et al.* 2013). These new models include a more complete understanding of the effect of the electrical double layer. For instance Pride (1994) ignored the effect of the Stern layer (the inner portion of the electrical double layer) and ignored induced polarization effects as discussed in the introduction of his paper. Therefore the frequency dependence of its electrical conductivity expression cannot be compared to any experimental data since the most important part of the physics is not in his model. We know however that the frequency dependence of electrical conductivity, and the relationship between the quadrature and surface conductivity can only understood in the context of a more elaborate theory as recently discussed in detail by Revil (2013a,b) and Revil *et al.* (2014b).

Table 2. Mesh grid size for *x*-axis, *y*-axis and time.

	Unit	Origin	Increment	Number of cells
x-Axis	metres (m)	0	1×10^{-3}	801
y-Axis	metres (m)	0	1×10^{-3}	801
Time	seconds (s)	0	1×10^{-7}	4001

Other differences appear between the theory developed by Revil, Jardani and co-workers and Pride theory, at least in the way this last model is usually implemented. Jardani *et al.* (2010), showed that we can solve for the displacement vector and fluid pressure using the Biot theory and then solving for the steaming potential in the quasi-static limit of Maxwell equations (Revil & Linde 2006). This approach is much more efficient than solving for the displacement vectors of the solid and fluid phases and then solving the electromagnetic diffusion equations in which induction is accounted for. Indeed, the number of unknowns for a 3-D seismic problem decreased to four (three for the displacement vector of the solid phase and one for pore fluid pressure).

Finally, Revil, Jardani and co-workers based their model on the use of a volumetric excess charge density of the pore space to model the electrokinetic effects rather than using the zeta potential as done in Pride's theory (e.g. Revil *et al.* 2013). This formulation allows to use an additional relationship between the effective charge density dragged by the flow of the pore water and permeability (Jardani *et al.* 2007). Since Biot theory is not able to capture various attenuation mechanisms existing in porous materials (such as squirt-flow mechanisms), simplification of the constitutive theory might be possible such as the poroacoustic approach discussed by Sava & Revil (2012), Revil *et al.* (2014a), and Sava *et al.* (2014). This approach puts more attention on the kinetics of the phenomenon rather than on the magnitude of the converted seismoelectric field. The new approaches developed by Revil, Jardani and co-workers can be applied to partially saturated porous media and multiphase flow while this is not the case of Pride's theory (Revil *et al.* 2007, 2014a; Revil & Mahardika 2013) despite some recent attempt to empirically extend Pride's theory to unsaturated conditions (Warden *et al.* 2013 and see associated discussion in Revil *et al.* 2014a).

As mentioned briefly above, field and laboratory experiments have shown that the interface response generated from one seismic source has generally much lower amplitude with respect to the coseismic signal and can be measured remotely with a signal-to-noise ratio depending on the background noise level and signal attenuation. There are few exceptions in field conditions when the ground close to the recording electrodes is quite dry and the coseismic effects pretty small. In addition, the conversion strength ranges from microvolts up to few millivolts (e.g. Butler *et al.* 1996; Haartsen & Pride 1997; Garambois & Dietrich 2002; Dupuis *et al.* 2007; Haines 2004; Zhu *et al.* 2008). The code developed by Grobbe *et al.* (2012)

Table 1. Mechanical, electrical and hydraulic properties of the sandstone core, surrounding water and the tank boundary.

Property	Symbol (Unit)	Core	Water	Plastic boundary
Bulk modulus	K_b (Pa)	2.2×10^{10}	2.2×10^{9}	5.0×10^{9}
Density	ρ (Kg m^{-3})	2300	1000	910
Conductivity	σ (S m^{-1})	0.2	0.03	0.001
Log permeability	$\mathrm{Log}_{10}k_0$ (log[m^2])	–12	0	0
Compression wave velocity	V_p (m s^{-1})	3100	1480	2300

Downloaded from http://gji.oxfordjournals.org/ at Colorado School of Mines on July 1, 2015

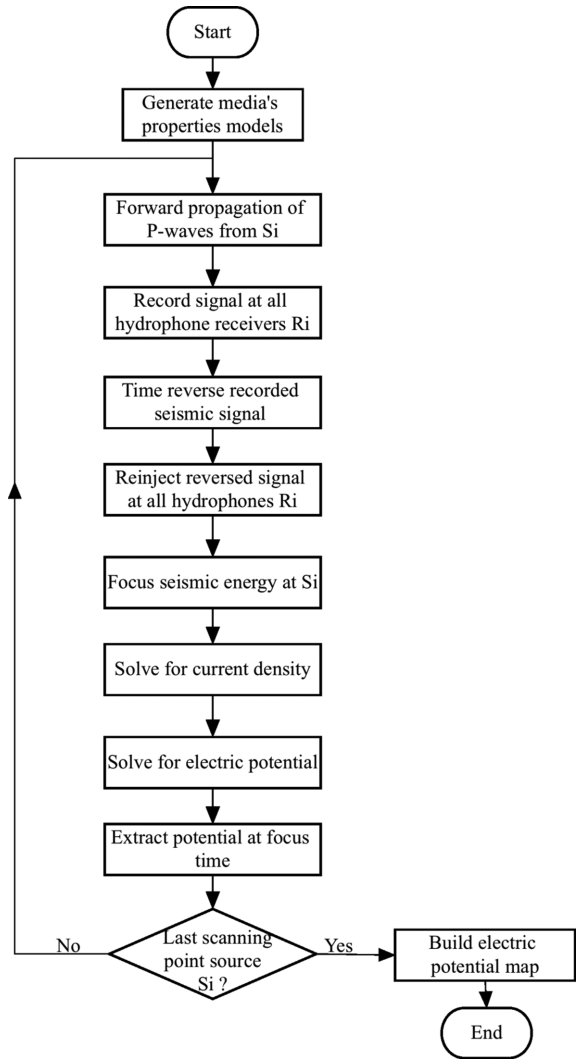

Figure 2. Flow chart summarizing the numerical procedure for the seismoelectric beamforming imaging technique. The goal of this technique is to produce a voltage map imaging the heterogeneities of the medium.

can also be used to generate all required fields for the theoretical interferometric seismoelectric Green's function retrieval. This can theoretically allow for instance to improve the signal-to-noise ratio of the weak seismoelectric conversions (or interface response fields). By applying interferometric techniques (e.g. de Ridder *et al.* 2009; Schoemaker *et al.* 2012), stacking inherently takes place with possible signal-to-noise ratio improvements.

In order to enhance the seismoelectric conversions with respect to the coseismic fields, Sava & Revil (2012) proposed to use multiple delayed in time seismic sources in order to focus the seismic wavefields at a given location, which will generate a higher pressure at the focus point due to the constructive interference of the wavefields compared to a single seismic source. If the focus point coincides with a mechanical, electrical and/or hydraulic discontinuity, a stronger interface response (electric field) is generated and recorded remotely. However, if the focus point belongs to a homogeneous medium, no electric response is expected at focus time. In addition, using multiple seismic sources, seismoelectric conversions will occur everywhere in the media where there is a discontinuity, but the highest intensity will be related to locations characterized by the largest gradient of material properties, especially electrical conductivity and permeability, which may vary over several orders of magnitude from one material to the other (Sava & Revil 2012). Using delayed in time seismic sources to focus the seismic energy at a set of specific locations, for instance on a regular grid, an electric potential map can be generated and used as an input for image-guided inversion in resistivity tomography (Sava *et al.* 2014).

There are however several aspects of the approach developed by Sava & Revil (2012) that were untested including the resolution of the method and the effect of an incorrect velocity model. In this paper, we numerically simulate a fictitious laboratory experiment composed of a fully water-saturated porous core submerged vertically in a circular water filled tank using the seismoelectric beamforming imaging technique. We analyse the efficiency of this method to image heterogeneous materials, examine the effect on incorrect velocity models on the output electric potential map and investigate the structural resolution of the seismoelectric image with respect to changing the wavelength of the seismic source.

2 BACKGROUND THEORY

2.1 Electrical double layer

During the propagation of seismic waves, the pore water moves with respect to the solid grains. The drag of the excess of charge of the electrical diffuse layer coating the surface of the grains (Gouy 1910; Chapman 1913) generates an electrical current of electrokinetic nature called the streaming current $\mathbf{J}_s$ (Pride 1994) Then, this current generates electromagnetic disturbances, which can be modelled thanks to the Maxwell equations, or, quite precisely, within their low-frequency approximation neglecting dielectric polarization and induction effects as discussed for instance in Jardani *et al.* (2010). These electromagnetic disturbances have dual character: local ones associated with the seismic waves themselves and interface conversions especially in presence of contrasts in electrical conductivity and permeability.

2.2 Dynamic poroacoustic wave modelling

The seismoelectric beamforming technique can be simulated using *P* waves, *S* waves or both in an elastic porous medium. However, for simplicity and reduction of the overall computational time, the seismoelectric problem is adapted and defined below within the acoustic approximation where the seismic wave is described in terms of either pressure perturbations or fluid displacement (Sava & Revil 2012; Revil *et al.* 2013). The confining pressure, P (considered positive in compression) corresponds to the trace, sum of the main diagonal elements, of the macroscopic stress tensor, $\bar{\bar{\mathbf{T}}}$, using the following relationship:

$$P = -\frac{1}{3} trace\left(\bar{\bar{\mathbf{T}}}\right) = -\frac{1}{3}\sum_{i=1}^{n} T_{ii}, \tag{1}$$

where 'trace' defines the trace operator of the matrix representation of the tensor. Moreover, the confining pressure P can be determined at any given time and location using the acoustic wave equation defined as:

$$\frac{\partial^2 P}{\partial t^2} - K_u \nabla \cdot \left(\frac{1}{\rho}\nabla P\right) = S(\mathbf{x}, t), \tag{2}$$

where K_u denotes the undrained bulk modulus of the porous material (Pa), ρ is its mass density (kg m^{-3}), $\mathbf{x}$ denotes the position

Downloaded from http://gji.oxfordjournals.org/ at Colorado School of Mines on July 1, 2015

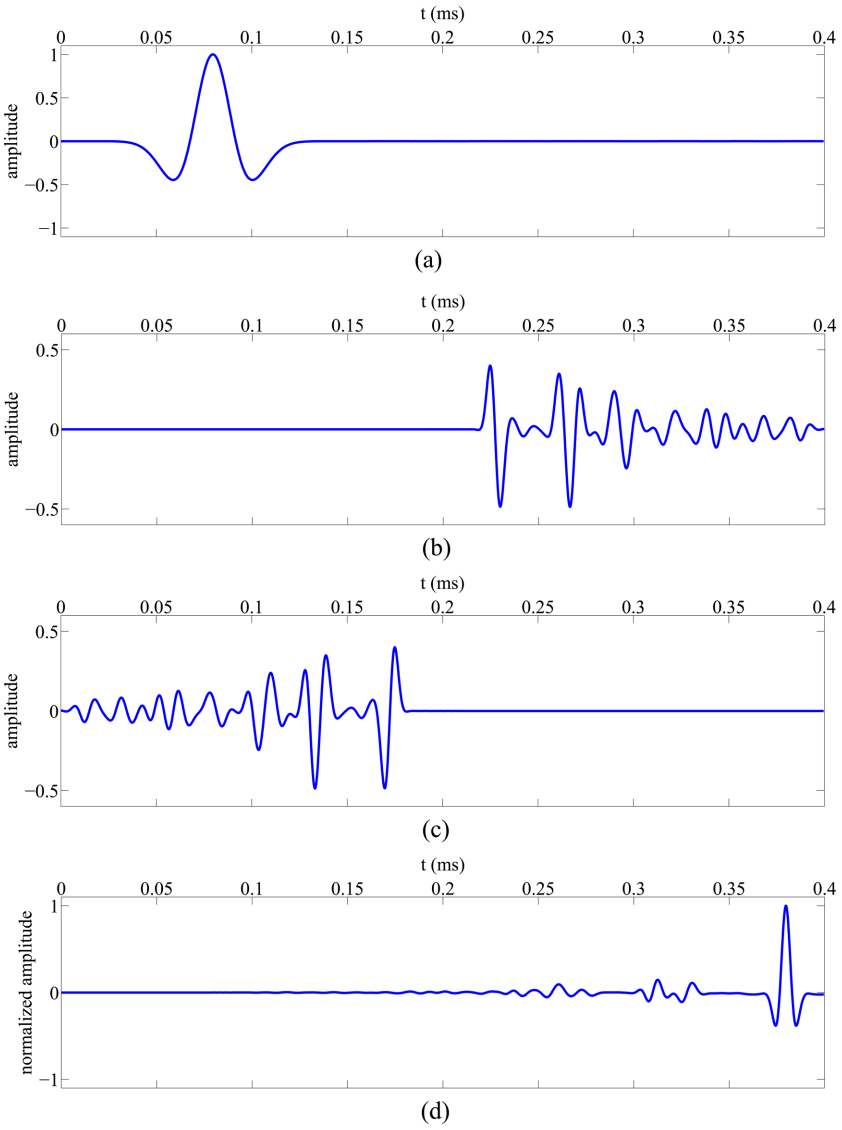

Figure 3. Input and recorded seismograms by source/receiver hydrophones. (a) Ricker wavelet with 75 kHz frequency (2 cm dominant wavelength in water) and time-shift of 0.08 ms, (b) waveform recorded at hydrophone (15 cm, 40 cm) during *P*-wave forward propagation, (c) reversed in time waveform recorded at hydrophone (15 cm, 40 cm) and (d) wavefield recorded at point source (47.5 cm, 44.5 cm) with highest normalized amplitude at focus $t = 0.38$ ms.

of the source in space (m), t represents time (s) and $S(\mathbf{x},t)$ is the acoustic source (Pa s^{-2}) that can be represented as a seismic point source using the following relation:

$$S(\mathbf{x}, t) = \delta(\mathbf{x} - \mathbf{x}_0)\, s(t), \tag{3}$$

where $\delta(\mathbf{x} - \mathbf{x}_0)$ is a delta function, $\mathbf{x}_0 = (x_s, y_s)$ the point source location and $s(t)$ is the time function of the source (Pa m^3 s^{-2}). In the following, we will use a Ricker wavelength for the source.

2.3 Electrokinetic theory

In the electrokinetic theory, coupling terms between mechanical equations and Maxwell's equations relate the electric fields to the seismic perturbations. These coupling coefficients are related either to seismoelectric, where the seismic wave propagation generates electromagnetic disturbance, or electroseismic, where an oscillatory electric field applied to a porous medium creates fluid flow (mechanical disturbance). In this section, we discuss how to couple the output pressure field from the wave equation with Darcy's law and Ohm's law to obtain the electric field in time and space.

2.3.1 *Generalized Darcy's law*

The pressure fluctuation due to the propagation of compressional seismic waves causes pore fluid pressure in the porous material to change which in turn leads to pore fluid flow. Darcy's law governs this relation by the following expression (neglecting high frequency inertial effects):

$$\dot{\mathbf{w}} = -\frac{k_0}{\eta_w}\nabla p, \tag{4}$$

where $\dot{\mathbf{w}}$ denotes Darcy's velocity (m s^{-1}) (flux density of water through the porous material), k_0 is the (low-frequency) permeability (m^2) of the porous medium to water, η_w is the dynamic viscosity (Pa s) of water and p is the pore fluid pressure (Pa). The pore fluid pressure is related to the confining pressure in the undrained regime

Downloaded from http://gji.oxfordjournals.org/ at Colorado School of Mines on July 1, 2015

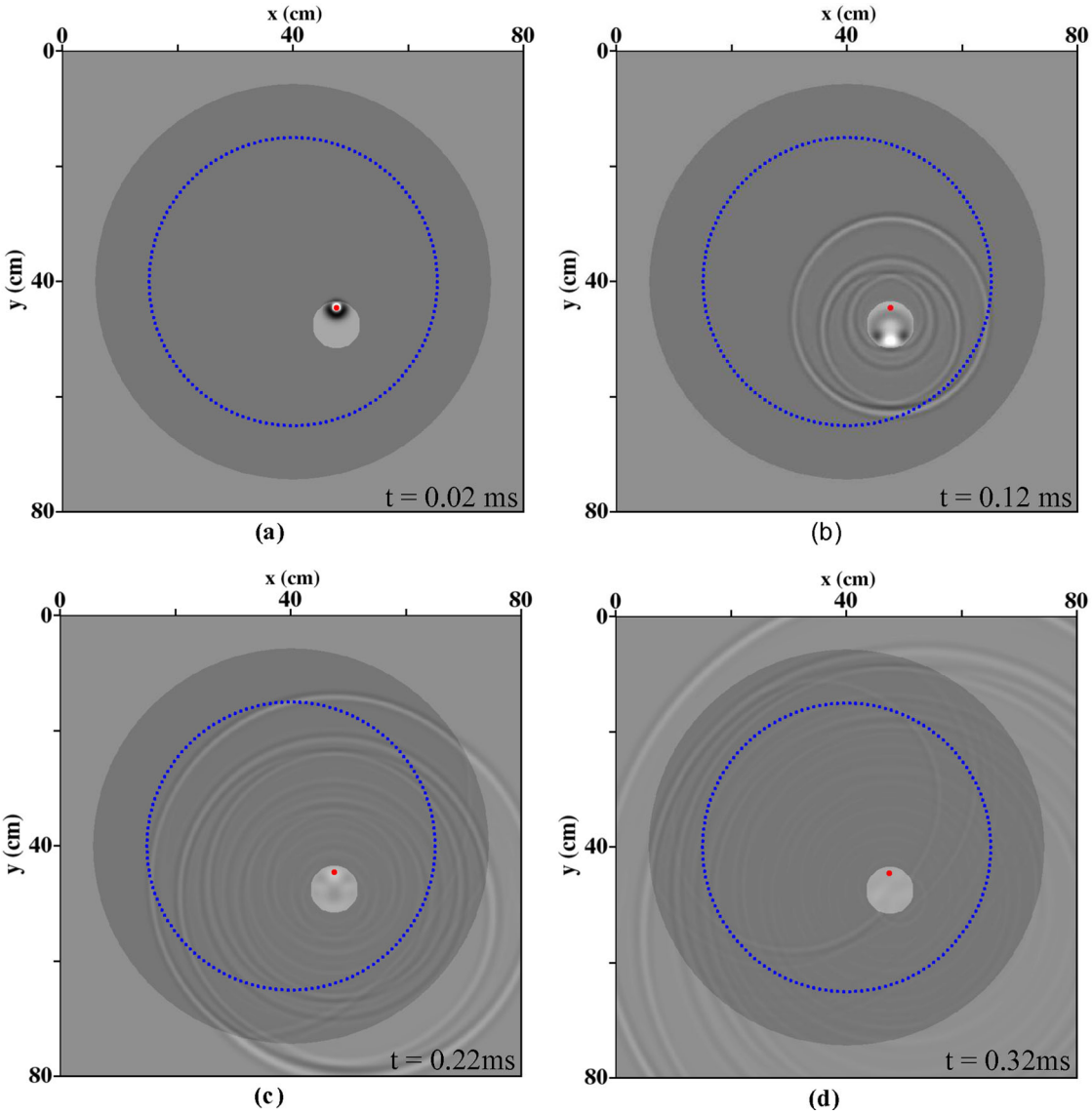

Figure 4. Forward propagation of the *P*-wave from a point source indicated by the red dot (47.5 cm, 44.5 cm) and recorded by the hydrophone receivers (blue dots) starting at 0.02 ms until 0.32 ms with 0.1 ms time increments.

of poroelasticity by $p = BP$, where B is the Skempton coefficient (unitless, $0 \leq B \leq 1$) given by:

$$B = \frac{1 - K/K_u}{1 - K/K_s}, \tag{5}$$

where K is the bulk modulus of the porous material (Pa) (drained bulk modulus of the skeleton with no fluid in the pores), K_u undrained bulk modulus (Pa) and K_s is the bulk modulus of the solid material (Pa) (we have $K_\mathrm{s} \geq K_\mathrm{u} \geq K$). Hence, eq. (4) can be express as:

$$\dot{\mathbf{w}} = -\frac{k_o}{\eta_w} \nabla (BP). \tag{6}$$

2.3.2 *Generalized Ohm's law*

The total electric current density $\mathbf{J}_{total} = \mathbf{J}_c + \mathbf{J}_s$ (in A m^{-2}) is the sum of the conduction current density, $\mathbf{J}_c = \sigma \mathbf{E}$ (σ the electrical conductivity and $\mathbf{E} = -\nabla\psi$ is the quasi-static electrical field, and ψ is the electric potential) and a source current density, $\mathbf{J}_\mathrm{s}$, given by:

$$\mathbf{J}_s = \hat{Q}_V \dot{\mathbf{w}} = -\hat{Q}_V \frac{k_0}{\eta_w} \nabla p, \tag{7}$$

where $\hat{Q}_V$ denotes the effective excess volumetric charge density (C m^{-3}) dragged by the pore fluid flow relative to the grains. Indeed, the pressure-induced pore fluid flow drags the excess counterions in the diffuse layer and generates an electrical source current density due to the charge imbalance between the pore fluid counterions and grain surface ions according to Jardani *et al.* (2010). In addition, knowing the permeability of the medium, the volumetric charge density parameter is obtained by using $\log_{10}(\hat{Q}_V) = -9.23 - 0.82\log_{10}(k_0)$ (Jardani *et al.* 2010; Revil & Jardani 2010; Revil & Mahardika 2013). Using the previous constitutive equations with the conservation of charge yields the following

Downloaded from http://gji.oxfordjournals.org/ at Colorado School of Mines on July 1, 2015

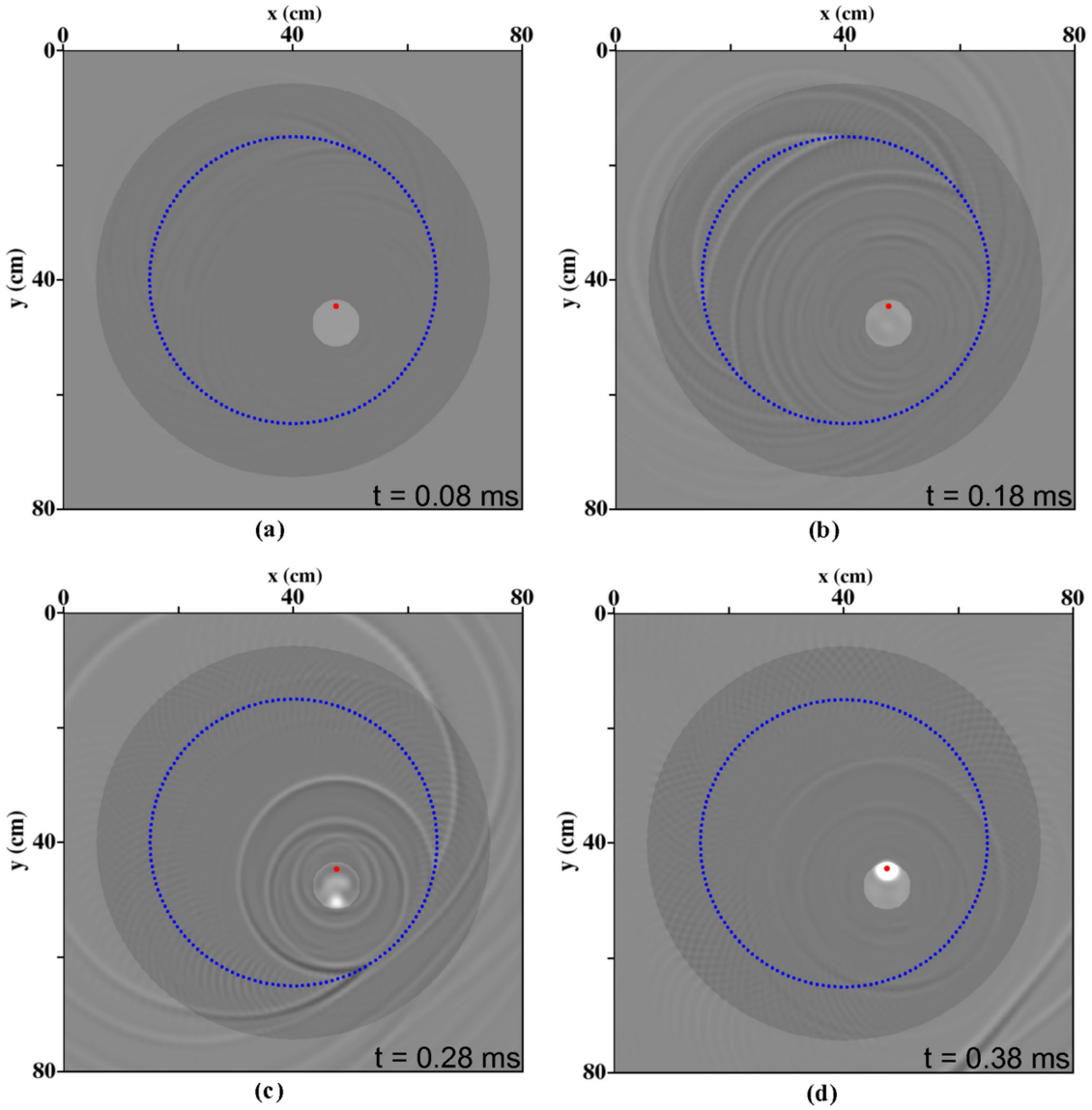

Figure 5. Re-injection of time reversed seismic signal at the hydrophones (blue dots) starting at time 0.08 ms until 0.38 ms with 0.1 ms time increments between snapshots where (d) corresponds to seismic wavefields focusing at source point (red dot) at $t = 0.38$ ms.

equation for the electrical potential (see Sava & Revil 2012 for details):

$$\nabla \cdot (\sigma \nabla \psi) = \nabla \cdot \left[-\hat{Q}_V \frac{k_o}{\eta_w} \nabla (BP) \right]. \tag{8}$$

The source term in eq. (8) connects the electrical problem to the seismic problem. Furthermore, eq. (8) shows how the heterogeneities in permeability and Skempton coefficient generate radiative electrical fields that can be instantaneously measured by electrodes in the medium (Sava & Revil 2012).

3 APPLICATION TO A SIMPLE FICTITIOUS LABORATORY EXPERIMENT

3.1 2-D model

Our numerical experiment is inspired from the laboratory tank experiments presented by Zhu *et al.* (2008) and Schakel *et al.* (2011). In both experiments, the authors were able to detect a seismoelectric signal while having the seismic source, electrode and sample interface belonging to the same plane. There were no seismoelectric effects detected in absence of the porous material and in presence of a porous sample, the electrical signals was shown to be due to the interface response (seismoelectric conversion). Our model includes multiple seismic sources located on a circular array surrounding a cylindrical core sample.

The 2-D model for the numerical analysis consists of 80 cm × 80 cm solid square tank with 70 cm diameter circular opening at the centre of it. The tank is assumed to be made of plastic and a 7.5-cm-diameter porous core sample is centred on position $(x_c, y_c) = (47.5 \text{ cm}, 47.5 \text{ cm})$ (Fig. 1). Electrode E1 is located at position $(x_1, y_1) = (35 \text{ cm}, 45 \text{ cm})$ while the reference electrode (E2) is located at infinity (Fig. 1). In addition, there are 150 source–receiver hydrophones located on a 50-cm-diameter circle centred on $(x_h, y_h) = (40 \text{ cm}, 40 \text{ cm})$. During forward propagation of the seismic field, a virtual point source, located at position (x_i, y_i), generates an acoustic wave. This seismic wave propagates in the medium and is recorded

Downloaded from http://gji.oxfordjournals.org/ at Colorado School of Mines on July 1, 2015

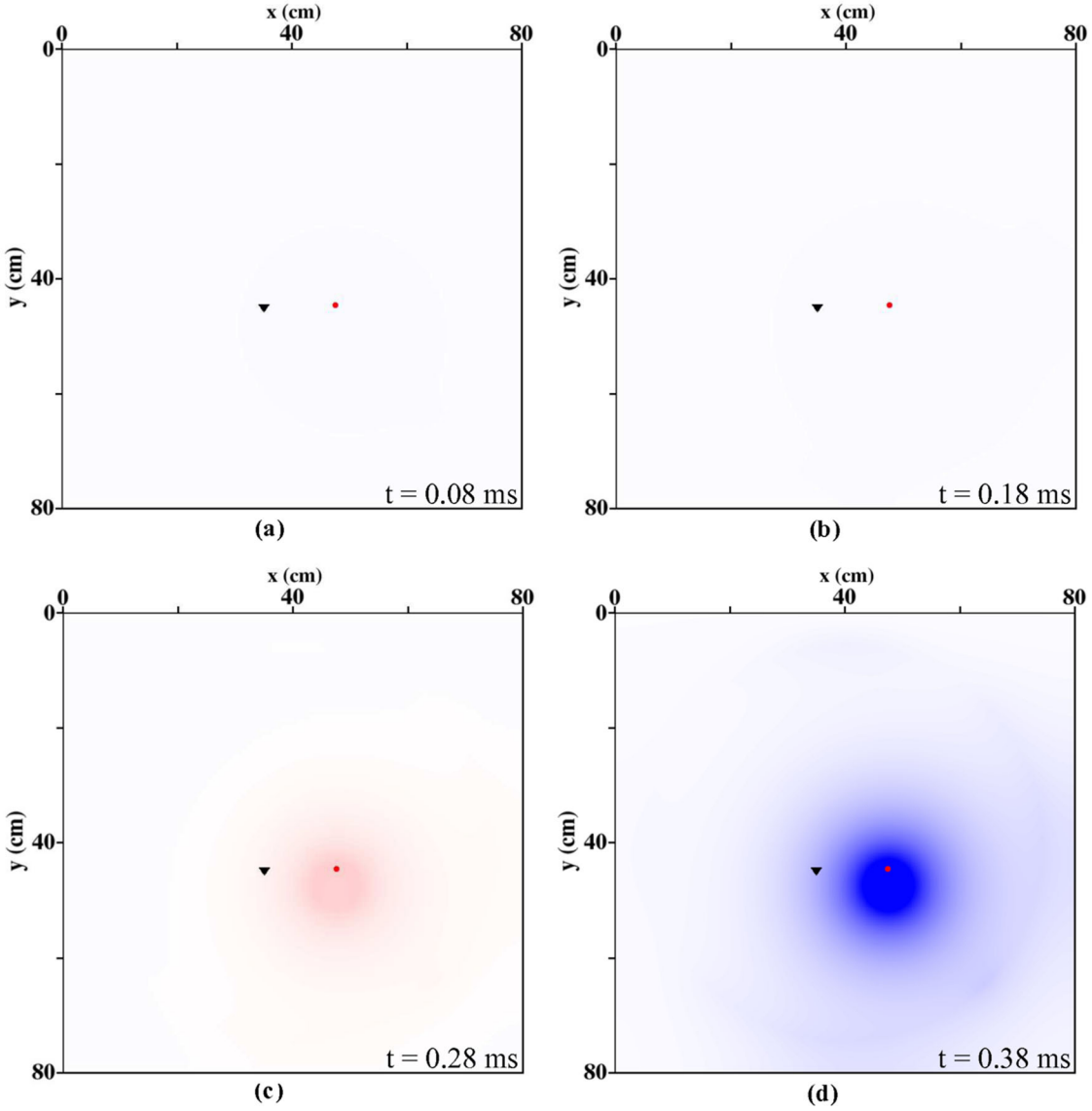

Figure 6. Electric potential map corresponding to the four snapshot of Fig. 7 where the red dot is source point (47.5 cm, 44.5 cm) and light blue triangle is electrode E1 (35 cm, 45 cm). Reference electrode (E2) is located at infinity. We do not plot the scale of the electrical potential because they depend on the intensity of the seismic source, which is arbitrary. The only thing that matters is that the relative change in strength of the electrical potential between any two snapshots.

by the circular array of the hydrophones. During time-reversal, the recorded signals by each receiver are reversed in time and injected in order to focus the *P*-wave energy at the point source (x_i, y_i).

The constitutive equations that govern the theory of seismoelectric beamforming presented in Section 2 are solved in the numerical simulation using the finite difference approach in the time domain. At any selected position (x_i, y_i), the seismoelectric virtual electrode can be constructed by solving, (1) the acoustic wave equation (eq. 2), (2) electric source created due to the current density induced by seismic wave and finally and (3) solving for the quasi-static electric potential (eq. 8).

The 2-D model is composed of a fully water saturated sandstone core, a plastic circular boundary filled with water. The porous plug material properties represent a synthetic sandstone reservoir (Sava & Revil 2012). The *P*-wave velocity can be approximated using eq. (9) by neglecting the viscous effects between the pore fluid and solid phase,

$$V_p = \sqrt{\frac{K_u}{\rho}}. \tag{9}$$

Eqs (2) and (9) can be eventually modified to include the effect of the shear modulus. The dynamic viscosity of water is 10^{-3} Pa s at 25 °C. The mechanical, electrical and hydraulic properties of the porous material are provided in Table 1. The numerical modelling is simulated with a constant mesh element-size of $\Delta x = 10^{-3}$ m, $\Delta y = 10^{-3}$ m and $\Delta t = 10^{-7}$ s (Table 2). All results presented in this paper can be reproduced using the Madagascar open-source software (Fomel *et al.* 2013).

Downloaded from http://gji.oxfordjournals.org/ at Colorado School of Mines on July 1, 2015

3.2 Beamforming methodology

The seismoelectric beamforming numerical modelling approach is summarized by the flow chart shown in Fig. 2. The methodology presented in this section illustrates the five steps to obtain the electric potential at the focus point. We have selected the virtual source point located at position (47.5 cm, 44 cm) to illustrate the figures; however, the same process can be applied to any point of the domain.

Step 1: Generate a model: The initial step is to construct the mechanical, hydraulic, and electrical distributions for all the relevant material properties defined in Table 1.

Step 2: P-wave forward propagation: Then, the selected seismic source is injected at the scanning point with a Ricker wavelet (e.g. 75 kHz dominant frequency time-shifted with 0.08 ms) pulse for $s(t)$ over 0.4 ms duration (Fig. 3a). Then we solve the wave equation to compute the seismic wavefield through the material. The simulated seismic signals are recorded by the circular receiver hydrophones set. Fig. 4 displays four time snapshots displaying the wave propagation from virtual point source to receivers starting at 0.02 ms until 0.32 ms with 0.1 ms time increments between any two consecutive snapshots. Moreover, extracting the recorded seismic wavefield at the hydrophone located at position (15 cm, 40 cm) shows that the first arrival to this location occurred at 0.22 ms with multiple lower amplitude signals due to reflections between the core and water interface, as well as reflections caused by water–plastic boundary (Fig. 3b).

Step 3: P-wave re-injection using time reversal: The recorded seismograms at every receiver is reversed in time and re-injected in order to focus all the seismic energy at the original source scanning point. The re-injected signal is not a clear signal similar to the input pulse due to the model's heterogeneities that generate reflections generated by the velocity and density contrasts existing at both the core-water and plastic-water interfaces that are observed at every receiver (Fig. 3c). Hence, at the focus time, the highest seismic wave intensity is located at the scanning point with some scattered reflected seismic waves at various locations in the medium. Fig. 4 shows four time snapshots for seismic wavefields of the time reversed re-injected seismic signal starting at time 0.08 ms until 0.38 ms with 0.1 ms time increments between any two consecutive snapshots. Moreover, if a hydrophone would be placed at the virtual point source point (47.5 cm, 44.5 cm), the recorded seismogram would show a Ricker wavelet at the focus time $t = 0.38$ ms similar to input waveform as shown in Fig. 3(d). An alternative method for focusing at a certain point can be obtained by considering a linear superposition of appropriately time delayed seismic sources. However, this approach requires additional calculations in order to determine the exact time-delays for every single source at every scanning point.

Step 4: Electrical current source: As mentioned previously, during back-propagation of the recorded seismograms, the seismic wavefield propagates across the whole medium. During this propagation, seismoelectric conversions occur at locations characterized by discontinuities of electrical, mechanical and hydraulic properties such as the interface between the water and the porous core sample. The generated source current density is calculated at every time increment (t), using the right side of eq. (8), for the whole medium based on the pressure fluctuations resulting from the back-propagated signal using the finite difference method. Since the electrical field depends only on the position of the wavefield at a given time, it is not history-dependent and so the calculations of the current density can be done at any time independently of prior times. The output current density maps are globally normalized for all time increments by scaling them with the highest value in order to preserve the relative relationships between the potential at various times and locations while eliminating the effects of the arbitrary input source strength.

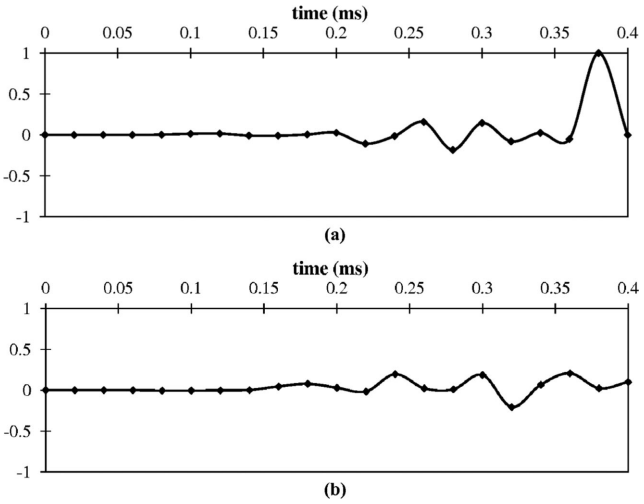

Figure 7. Electrograms. (a) Focusing at position (47.5 cm, 44.5 cm) located at the core–water interface. This focusing generates a high electric potential at the focus time ($t = 0.38$ ms) due to seismoelectric conversion at the interface between the water and the porous material. (b) Focusing at position (40 cm, 44.5 cm) located in water generates nearly no electrical potential at the focus time ($t = 0.38$ ms). The voltages are normalized using the voltage at the focusing time in the first case. The filled symbols represent the time at which the simulations are performed.

Step 5: Computation of the electrical potential at the focusing time: The electric potential is then calculated in order to determine the recorded voltage at any time (t) at the electrode with the reference voltage electrode located at infinity. Fig. 6 shows the corresponding electric potentials for the four wavefield snapshots in Fig. 5. As the seismic waves propagate through the core, seismoelectric conversion occurs; however, the interface response electric potential recorded by the electrodes at the focus point (Fig. 6d) has the highest amplitude if (and only if) it coincides with a heterogeneity. Therefore, extracting the recorded voltage at the electrode over the simulated time, Fig. 7a, shows that the greatest amplitude corresponds to the focus time ($t = 0.38$ ms). This is not always true however, for instance in the case where the focus point is located in a homogeneous material and the waves has passed through an interface earlier. The electric potential as a function of time is recorded for another scanning point at position (40 cm, 44.5 cm) located in water. As expected, the electric potential at this focus point is much smaller than in the previous case (Fig. 7b). In addition, the electrode records smaller voltages at times prior to the focus time compared to electric potential at focus time in Fig. 7a. These voltages are due to seismoelectric conversions as the seismic waves propagate through the medium and reach the porous core. In our case, we know the velocity model and therefore the focus time. If the velocity model would not be known, we would look for a maximum in the electrical potential for an estimated focus time related in turn to a prior velocity model.

Finally, in order to generate a seismoelectric image composed of electric potentials over a grid of scanning points, simulations should be done by repeating Steps 2 through 5 for each virtual source location and the electric potential at the focus time should be extracted for each scanning point.

Downloaded from http://gji.oxfordjournals.org/ at Colorado School of Mines on July 1, 2015

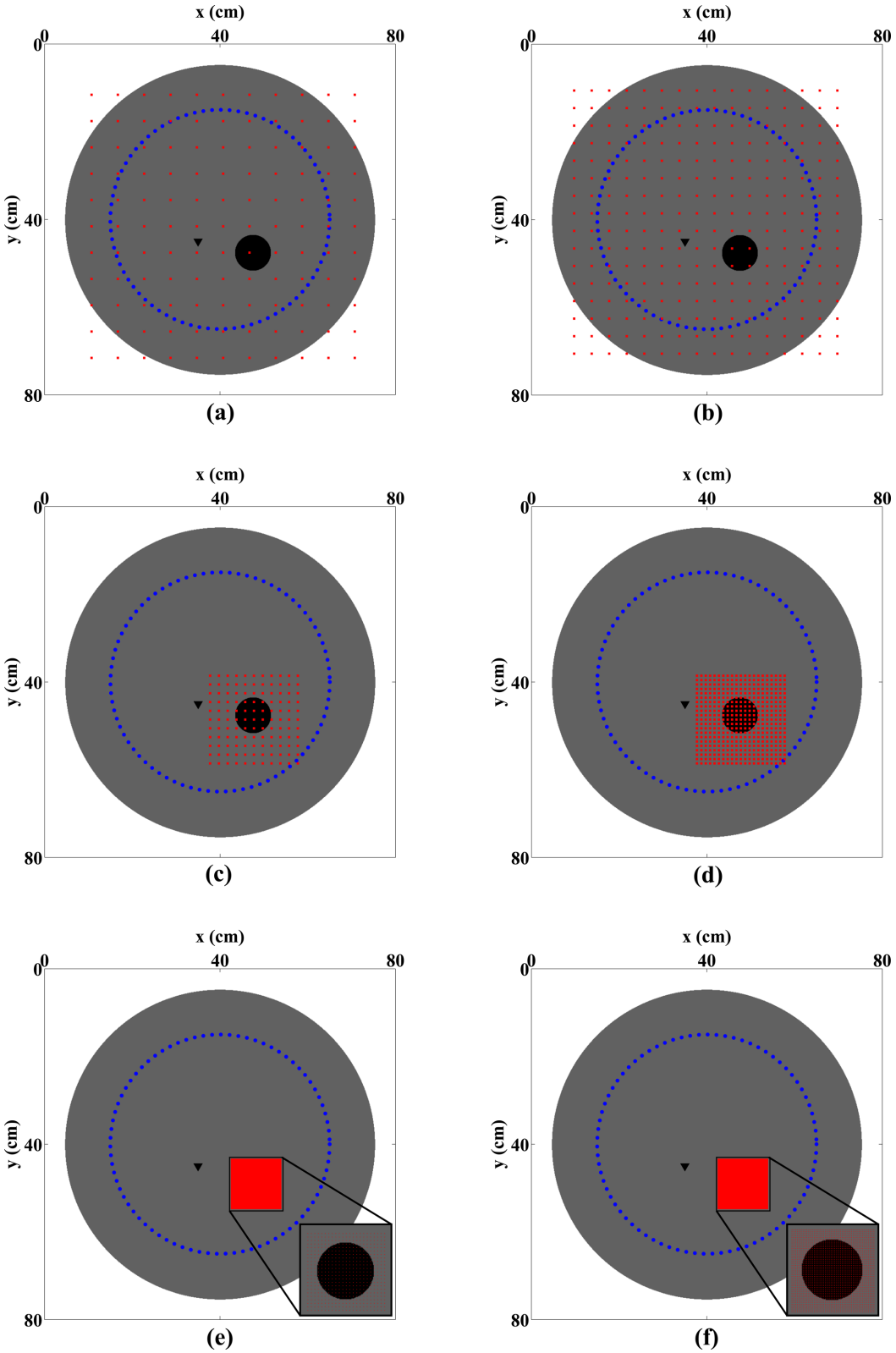

Figure 8. Coarse ($3 \times \lambda_{dom}$) to very fine ($\lambda_{dom}/8$) virtual point source grid. Simulated area for (a) and (b) is 60 cm × 60 cm, (c) and (d) 20 cm × 20 and (e) and (f) 11 cm × 11 cm with (a) 6 cm (b) 4 cm, (c) 2 cm (d) 1 cm (e) 0.5 cm and (f) 0.25 cm spacing between any two adjacent focus points.

3.3 Results and interpretation

The resolution of the seismoelectric beamforming maps or images is dependent on the density of the scanning points. However there is clearly an optimal choice depending on the frequency of the seismic wave itself. Before tackling this question in detail, we look at a scanning strategy using an iterative method to scan the medium, first with a coarse density of points, then refining the solution where

Downloaded from http://gji.oxfordjournals.org/ at Colorado School of Mines on July 1, 2015

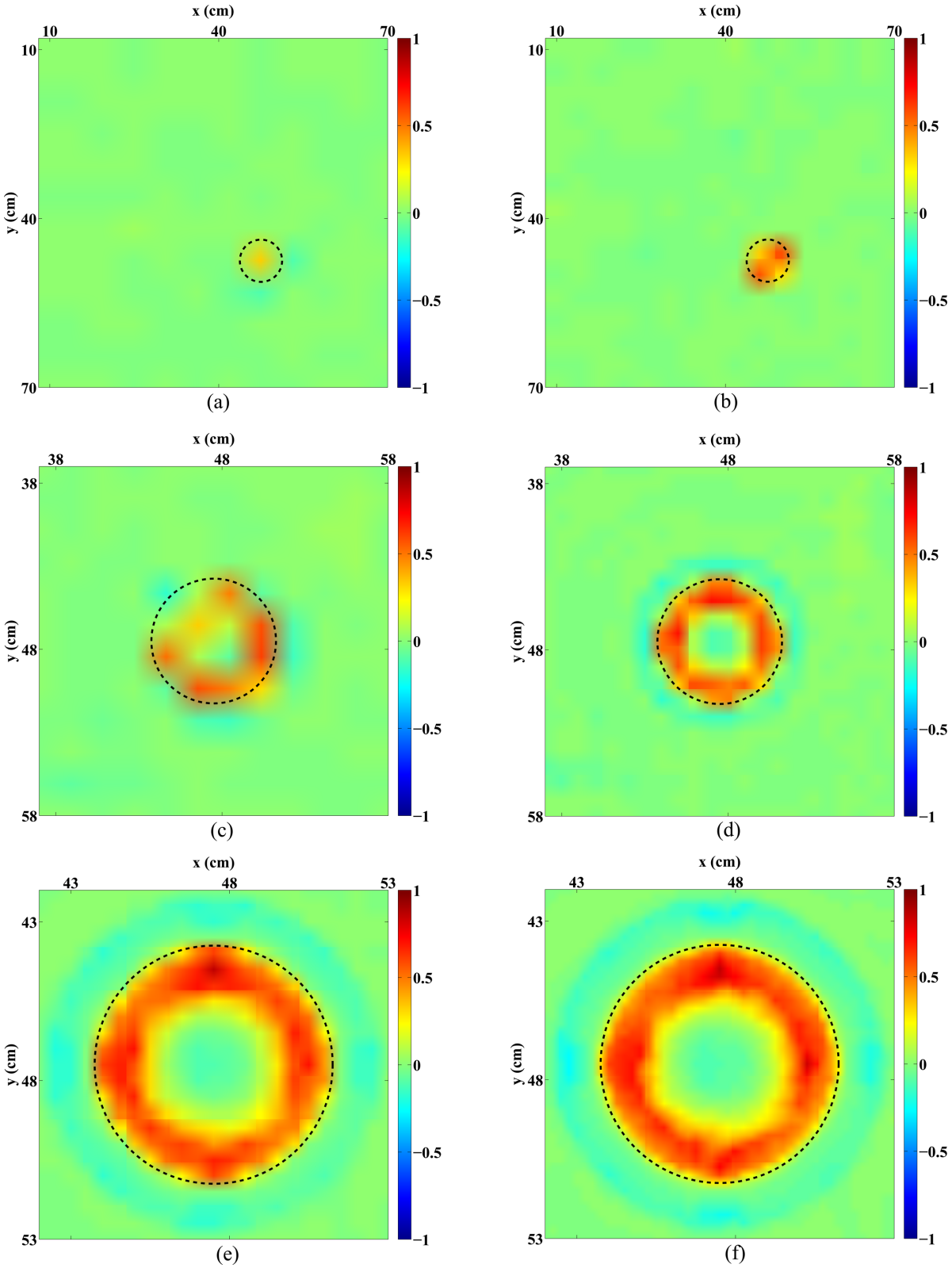

Figure 9. Seismoelectric voltage maps. Normalized electric potential corresponding to a virtual point source grid with (a) 6 cm (b) 4 cm (c) 2 cm (d) 1 cm (e) 0.5 cm and (f) 0.25 cm spacing, see Fig. 8, with true object circumference highlighted by the dashed black circle. With increasing space sampling the heterogeneous material contour and location is more visible and imaged clearly by the seismoelectric beamforming technique.

Downloaded from http://gji.oxfordjournals.org/ at Colorado School of Mines on July 1, 2015

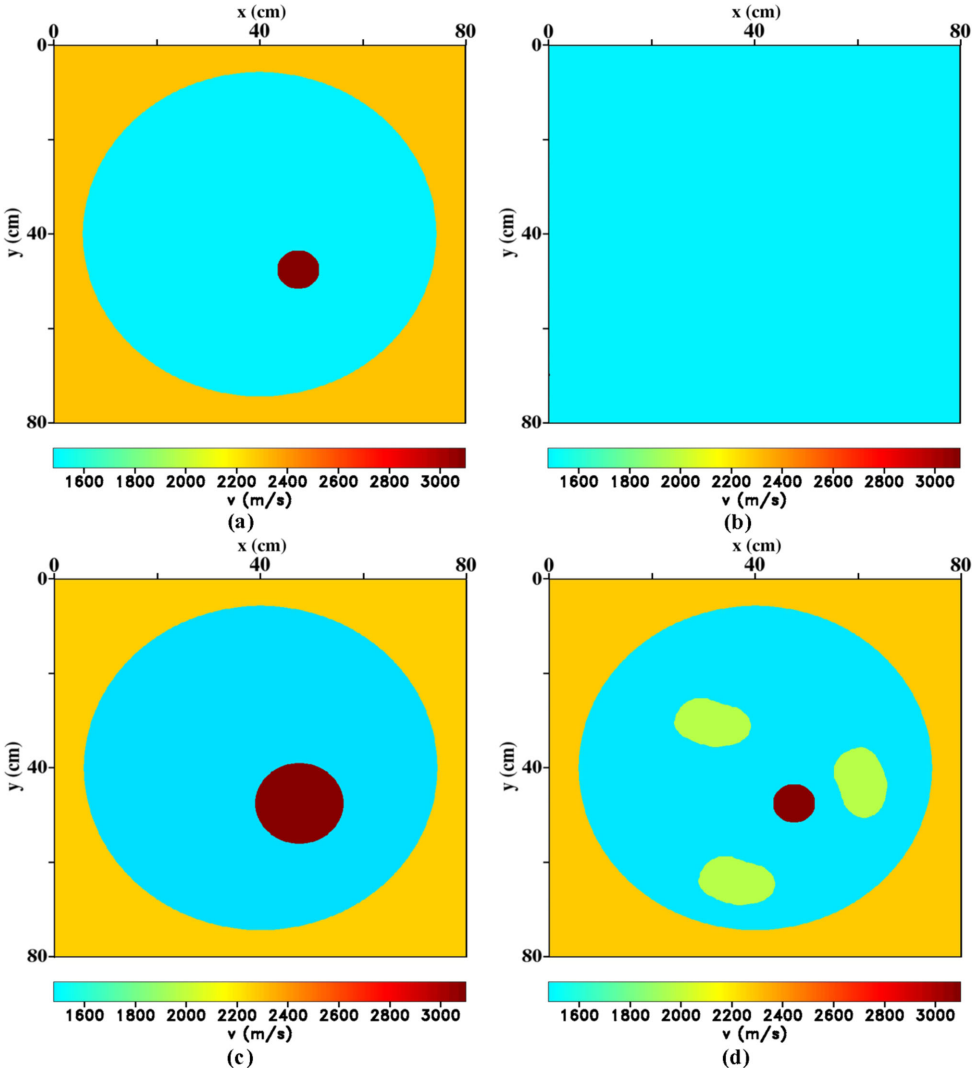

Figure 10. Analysis in the heterogeneous case without the knowledge of the velocity field. (a) True velocity model applied during forward *P*-wave propagation from virtual point source to circular hydrophone receiver array while the re-injection velocity models are either (b) constant water velocity (1480 m s^{-1}) (c) larger core model, and (d) other bodies with a 2000 m s^{-1} velocity.

anomalies are observed to increase the resolution at these points. For the following analysis, the source point spacing is proportional to the dominant wavelength in water (λ_{dom}).

In the first iteration, a coarse grid of 6 cm spacing ($3 \times \lambda_{dom}$, Fig. 8a) is chosen to scan quickly the majority of the model (60 cm × 60 cm) followed by a 4 cm spacing grid ($2 \times \lambda_{dom}$, Fig. 8b). Based on the normalized electric potential maps from the first two iterations (Figs 9a and b), a high amplitude anomaly is identified surrounding the position at 46 cm in x and y, which most likely is related to the presence of the porous core sample. In addition, the low electric potential values scattered in both maps is related to possible seismoelectric conversion between the water and sample boundary. Consequently, a smaller scanning region is identified (20 cm × 20 cm) around this potential target and scanned with a 2 cm resolution grid (corresponding to the wavelength λ_{dom}) of the seismic wave) and then a 1 cm resolution grid ($\lambda_{dom}/2$).

The third level of scanning utilized the 2 cm scanning resolution grid (Fig. 8c) and returned a low-resolution fuzzy image of the anomaly with respect to the background (Fig. 9c). However, decreasing the density of scanning point to a 1 cm resolution grid (Fig. 8d) produces an image of what appears to be a circular object (Fig. 9d). At this step, a preliminary conclusion on the shape of the core can be made, but the exact location and diameter of the object is still vague. Likewise, a smaller scanning area (12 cm × 12 cm) can be safely selected to enclose the anomaly and disregard areas of homogeneity (characterized by low electric potentials) to decrease the total computational time with finer grids of 0.5 cm grid spacing ($\lambda_{dom}/4$) and 0.25 cm grid spacing ($\lambda_{dom}/8$). Accordingly, the 0.5 cm scanning point grid (Fig. 8e) produced a high-resolution image of the porous core sample (Fig. 9e) and the diameter of the core, where the transition from negative to positive electric potential amplitude indicates the boundary, is approximately calculated to be 7.5 cm from the centre located at position (47.5 cm, 47.5 cm). Similarly, the latter observations are checked from the image resulting from the use of the finest scanning grid (0.25 cm resolution, Fig. 8f). Note also that since the core is modelled as a homogeneous material, the area inside the core sample exhibit vanishingly small electric potentials (Fig. 9f).

Downloaded from http://gji.oxfordjournals.org/ at Colorado School of Mines on July 1, 2015

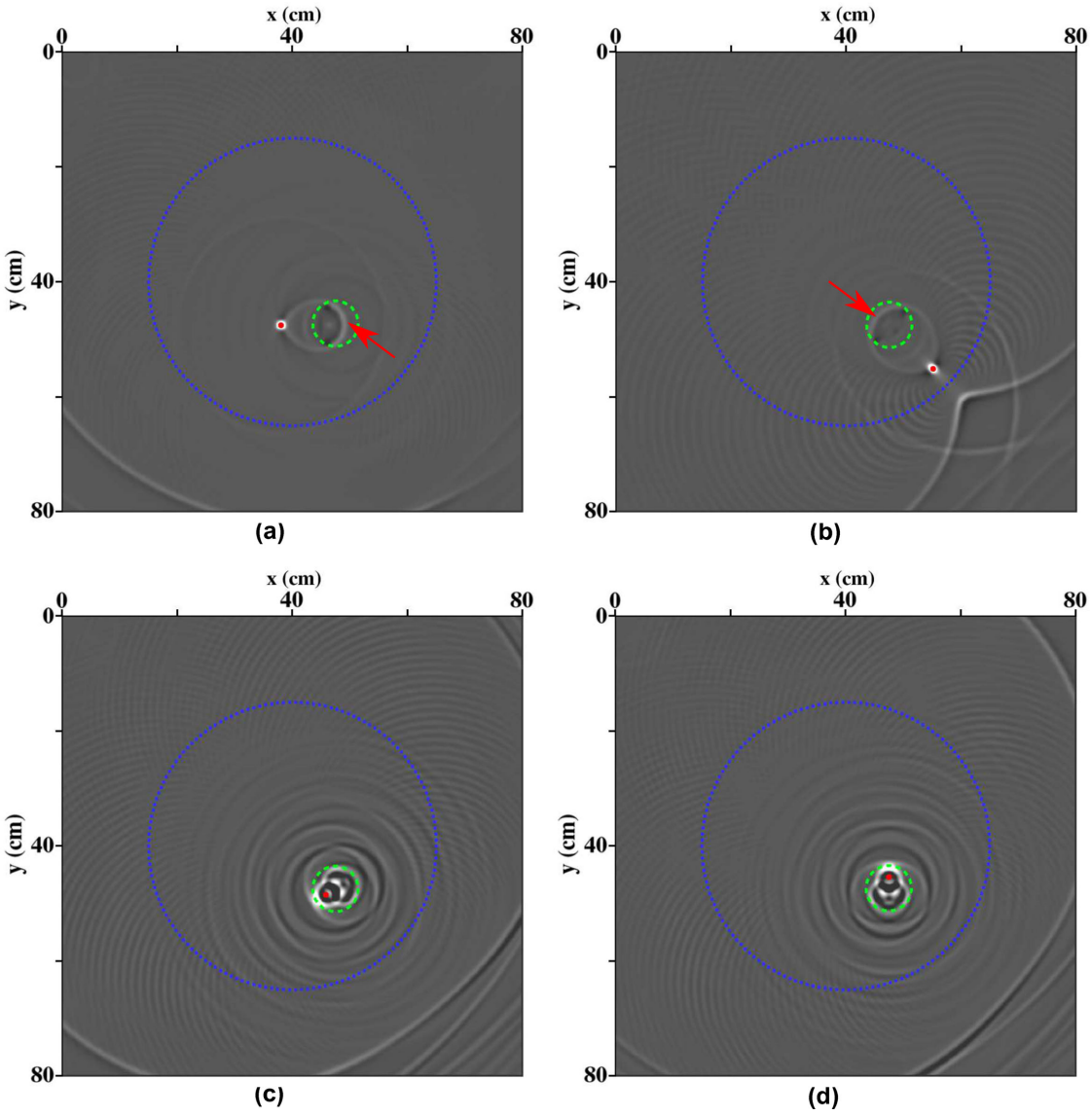

Figure 11. Seismic wavefields at focus time during *P*-wave reinjection with constant velocity model. Virtual point sources (red point) located in water zone (a and b) had wavefields focus at source location while the sources located inside the core (c and d) had seismic energy centre at a different position. The dashed green circle indicates the true core's circumference while the red arrows point out the seismic waves propagating through the core at focus time for source points located in the water zone.

In conclusion, the seismoelectric beamforming technique can be applied to image heterogeneities and produce high-resolution electric potential maps. Our experiment suggests that we need to have at least four to eight scanning points per wavelength in order to achieve a high definition seismoelectric image. On the other hand, if the distance between the scanning points is greater than the width or length of the object, this may result in skipping the anomaly by having the virtual source locations at homogeneous points that might lead to undetectable seismoelectric anomalies.

4 VELOCITY AND WAVELENGTH SENSITIVITY ANALYSIS

4.1 Velocity analysis

The seismoelectric voltage image produced with 4 scanning points per wavelength (0.5 cm source spacing) provided sufficient information to image the boundary of the porous core and to determine its shape, size and location (Fig. 9e). Therefore, for the simulations presented in this section, we considered the same 2-D model (Fig. 1), material properties (Table 1), and input source signal (Fig. 3a) during the forward propagation, but in the re-injection phase an incorrect velocity model is now applied. Our goal is to record true signals during forward modelling (using time reversal with an incorrect velocity model) but inaccurately process it through the velocity model during the re-injection step. This process would be similar to a typical field experiment in which the velocity model is not known precisely.

The scanning area for these simulations is 25 cm × 25 cm with x and y ranging between 35 and 60 cm, and we use 0.5 cm between two consecutive virtual point sources in the x and y directions. The plotted wavefields over the model, at focus times, are extracted for 2 points located in the water layer (38 cm, 47.5 cm) and (55 cm, 55 cm) and 2 points within the core (45 cm, 49 cm) and (47.5 cm, 44.5 cm).

Downloaded from http://gji.oxfordjournals.org/ at Colorado School of Mines on July 1, 2015

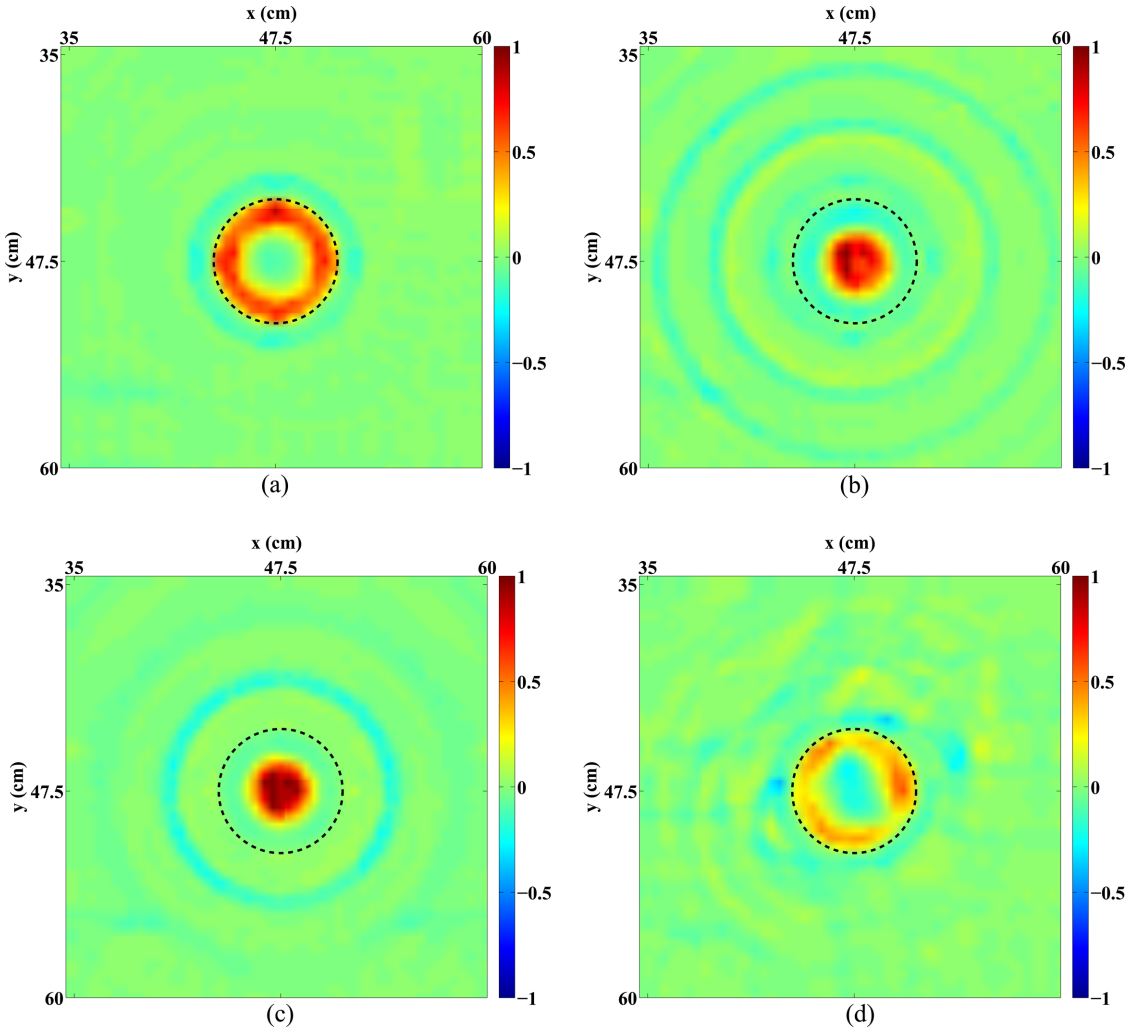

Figure 12. Seismoelectric voltage maps. Normalized electric potential map with from reinjection (a) true velocity model (b) constant velocity model (1480 m s^{-1}) and (c) larger diameter core model and (d) artificial velocity model. The dashed circle indicates the true position of the interface between the core sample and water.

4.1.1 Constant velocity model

In classic geophysical analysis, such as seismic data processing, when there is any missing information, the initial approximation in the first iteration would be an average constant value for the velocity based on the mean travel time between sources and receivers when the seismic wavefield crosses the medium. Accordingly, since the majority of the 2-D model is water, we selected a constant water velocity value of 1480 m s^{-1} to re-inject the *P*-wave waveform into the medium (Fig. 10b).

During the re-injection step, the virtual source points located in pure water zone have the seismic wavefields focus at the source location (Figs 11a and b) due to the fact that the true model and approximated model for the water layer are equivalent. However, when the source point coincided with the core, at the focus time the seismic wavefields concentration are shifted by few centimetres due to the velocity difference between core (3100 m s^{-1}) and velocity model (1480 m s^{-1}), refer to Figs 11(c) and (d). In addition, there are scattered *P* waves over the entire medium at the focus time due to the velocity difference of the models.

The recorded electric potential at the focus time, depending on virtual point source location in space and new velocity model, is extracted for the 2704 virtual point sources and plotted in Fig. 12(b). Comparing the result with the true exact model (Fig. 12a), the core's centre is at the correct location (47.5 cm, 47.5 cm) with a circular shape and correct diameter. However, the electric response within the core is distorted due to the incorrect seismic waves focusing position. Moreover, multiple rings characterized by decreasing amplitude with increasing diameter are identified. This phenomenon is related to the presence of propagating seismic waves through the core at the focus time (see Figs 11a and b) that generated relatively low interface response electric field that is recorded by the electrode.

4.1.2 Incorrect velocity model with a larger core model

The second velocity model is extracted based on the electric potential map from Section 4.1.1. In this model, the core is centred on position (47.5 cm, 47.5 cm) but with a 16 cm diameter that coincides with the first ring, as shown in Fig. 10(c). Similar to the

Downloaded from http://gji.oxfordjournals.org/ at Colorado School of Mines on July 1, 2015

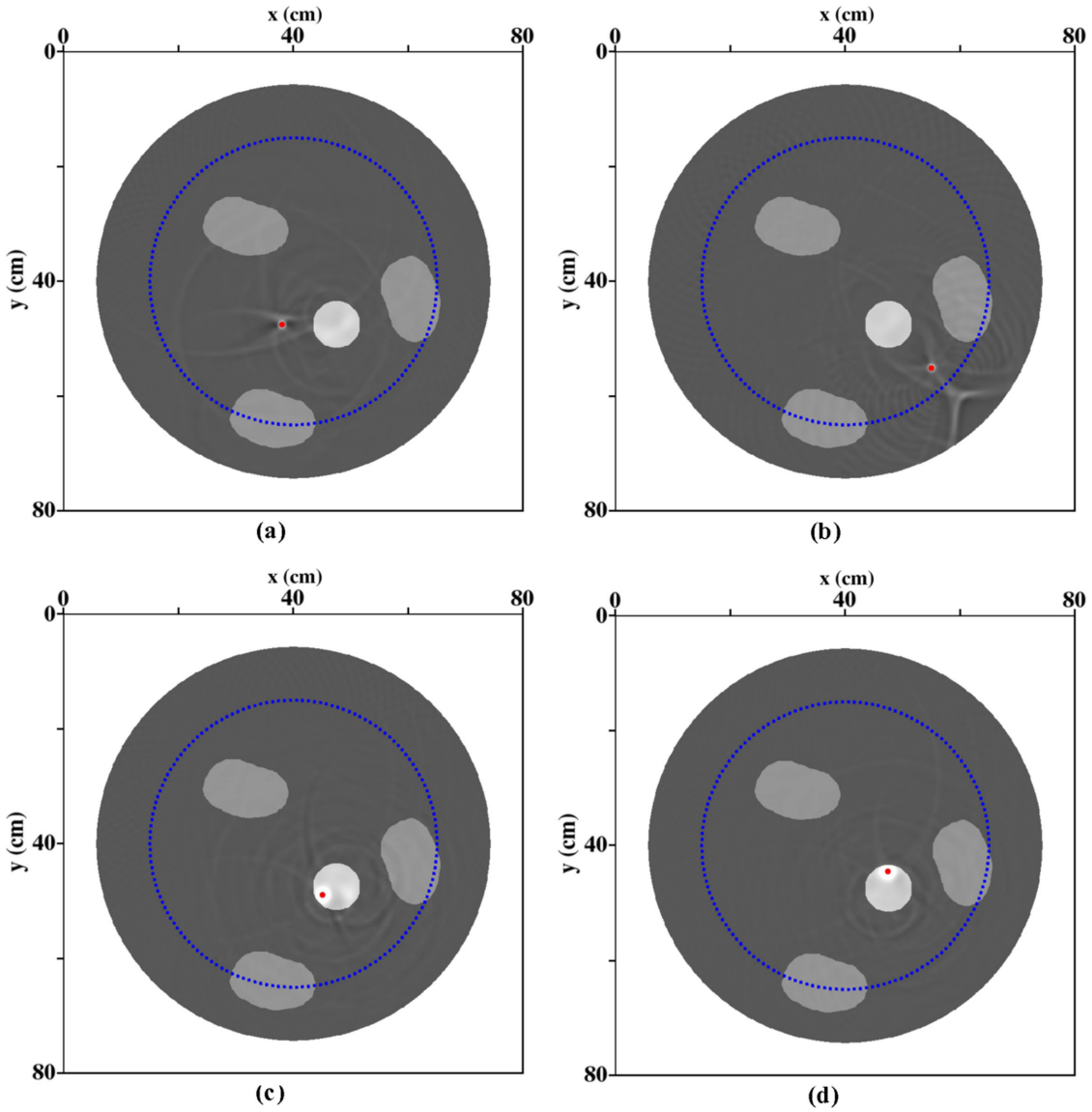

Figure 13. Seismic wavefields at focus time during *P*-wave reinjection using the three artificial 2000 m s^{-1} velocity model. Virtual point sources (red point) located in water zone (a and b) and inside the core sample (c and d) had the wavefields focus at the source point with some scattered waves due to the artificial velocity bodies.

previous simulation, at focus time the seismic energy focus location coincides with the virtual point source positioned in water. On the other hand, the seismic wave constructively superimposed a couple centimetres away from true position for point sources located in the core sample. Furthermore, there are scattered acoustic waves in the entire medium at focus time due to the velocity mismatch between true and estimated models. Consequently, the generated electric potential map (Fig. 12c) produced an improved image compared to the previous case where the multiple rings present around the core in case 1 (Fig. 12b) decreased to only one visible ring with 12 cm diameter. The core's centre is at the right location and the diameter is slightly smaller than true model. Therefore, additional iterations with smaller core diameter are required to refine the output image and generate an electric potential map closer to true model.

4.1.3 Incorrect velocity model by adding additional heterogeneities in the medium

In the final simulation, three bodies (with a *P*-wave velocity of 2000 m s^{-1}) are added to the true velocity model (Fig. 10d). At the focus time, the injected seismic waves constructively superimposed at the true virtual source position (see Fig. 13). The three bodies refracted and reflected the seismic waves throughout the whole medium resulting in smaller seismoelectric interface response whenever the *P* wave passed through the cylindrical core sample at the focus time. The electric potential map generated for this simulation shows a slightly skewed 7.5 cm diameter circular object corresponding to the core at the true location (Fig. 12d). Comparing the results with the exact model, the core's surrounding voltage map is characterized by relatively higher noise compared to the original true velocity results.

Downloaded from http://gji.oxfordjournals.org/ at Colorado School of Mines on July 1, 2015

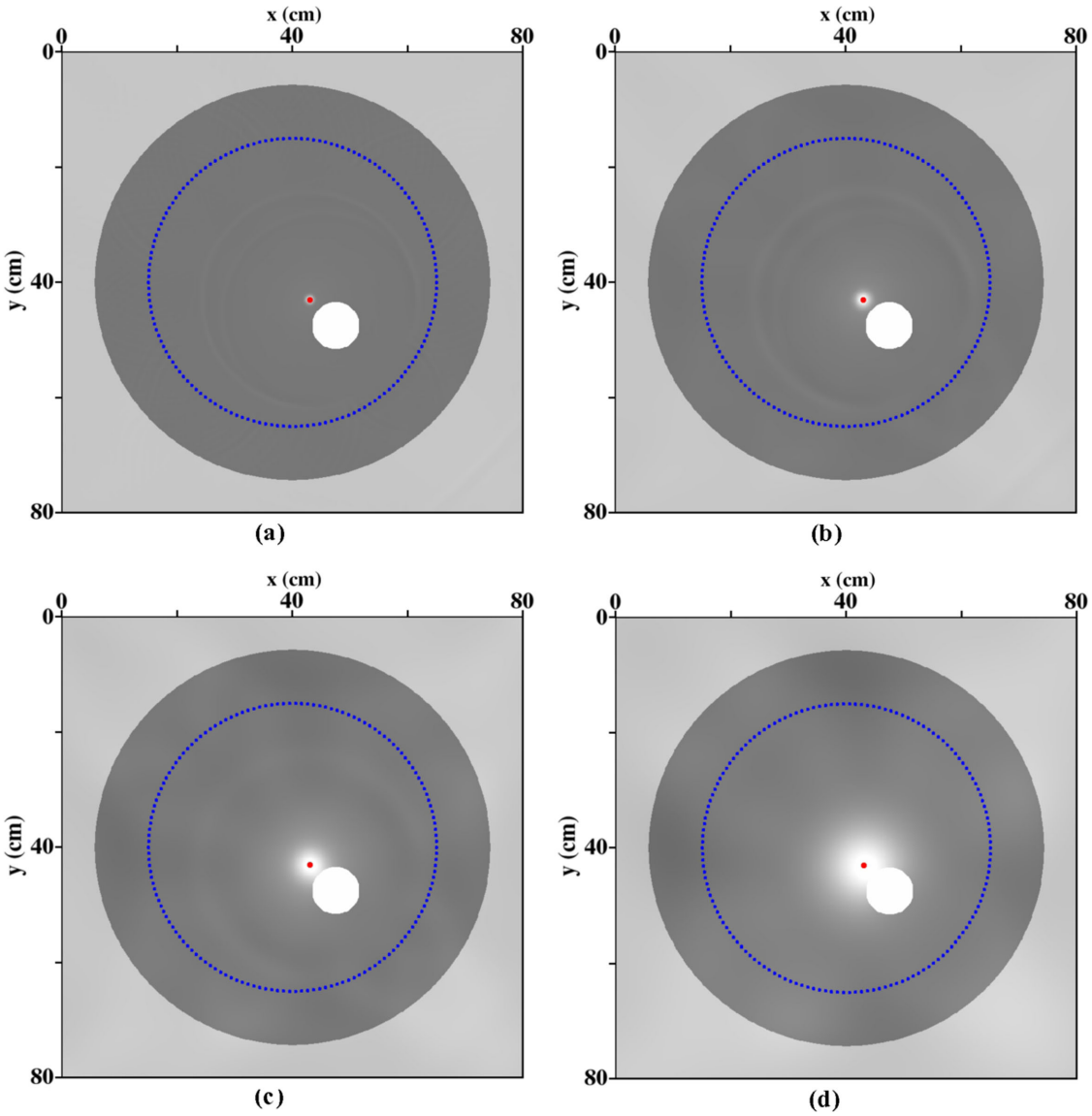

Figure 14. Seismic waves constructive superposition at the focus time for point (43 cm, 43 cm) with (a) 75 kHz (b) 37.5 kHz (c) 18.75 kHz and (d) 9.375 kHz dominant frequency Ricker wavelet input signal.

4.2 Wavelength analysis

The selection of the source's dominant frequency/wavelength plays a vital role in imaging porous material and is directly related to the dimensions of the object. Hence, we analyse the effect of source wavelength on the output voltage map. In this section, the 2-D model and material properties presented in Section 3 are simulated with four dominant Ricker wavelet frequencies (75, 37.5, 18.75 and 9.375 kHz), respectively. In addition, the scanning area is 25 cm × 25 cm starting at 35 cm to 60 cm with respect to origin. We use also a spacing of 0.5 cm between two consecutive virtual source points.

As the source's dominant frequency decreases, the corresponding wavelength increases and the extent of the seismic waves at the focus time becomes larger as demonstrated in Fig. 14 for point (43 cm, 43 cm) located in the water layer. The associated electric potential maps for each simulation are shown in Fig. 15. For the first case (75 kHz dominant frequency, 2-cm wavelength) the core object is imaged with high definition showing the correct location with a clear water/solid interface at 7.5 cm diameter. In the second case (37.5 kHz dominant frequency, 4-cm wavelength), the seismic waves coverage at focus time is slightly larger than case 1 (see Fig. 14b) that generates additional low amplitude interface response for water located point sources that is not present in the first case. These caused the thickness of the negative amplitude surrounding the core and positive amplitudes within the core to 'double' and generate a lower resolution image at the correct location but with a smaller diameter (approximately 6.5 cm compared to the true diameter of 7.5 cm), refer to Fig. 15(b). In the third simulation (18.75 kHz dominant frequency, 8-cm wavelength), the electric potential map predicted correctly the core's location and potential circular shape; however, the positive–negative boundary interface is not present any more, see Fig. 15(c). In the final simulation (9.375 kHz dominant frequency, 16-cm wavelength), the electric potential provided limited information on the shape and size of the porous material. The resolution is too low as shown in Fig. 15(d).

Downloaded from http://gji.oxfordjournals.org/ at Colorado School of Mines on July 1, 2015

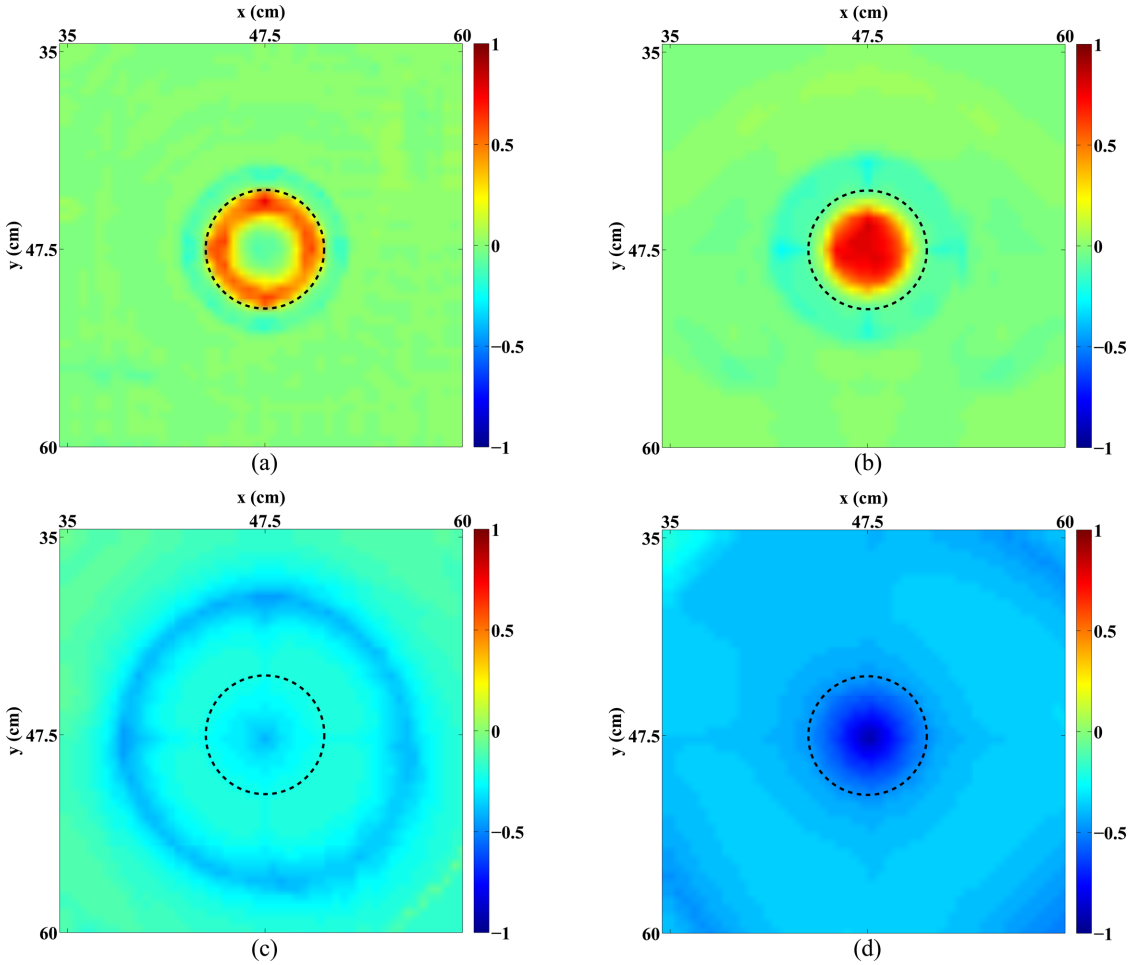

Figure 15. Seismoelectric voltage map. Normalized electric potential map corresponding to the four simulated dominant frequency sources shown in Fig. 15. (a) 75 kHz (b) 37.5 kHz (c) 18.75 kHz and (d) 9.375 kHz dominant frequency Ricker wavelet input signal. Note the change of polarity of the target obtained with a change of the frequency of the seismic wave.

Moreover, in order to examine the frequency effects on the output electric potential, we consider a modified 2-D model by removing the plastic boundary, placing a 10 cm diameter core on (40 cm, 45 cm) and electrode E1 on (40 cm, 20 cm) while reference electrode (E2) is located at infinity. The seismoelectric conversion takes place between the water-solid interface where a virtual point source is placed at position (40 cm, 40 cm) (Fig. 16a). For all simulations, the input signal is a Ricker wavelet with dominant frequency ranging between 35 and 150 kHz, a constant time-shift of 0.15 and 3 ms total simulation time. The electric potential recorded by the electrode at the focus time is extracted and plotted with respect to source dominant frequency as shown in Fig. 16(b). As the frequency increases, the energy at the focus time is more concentrated around the virtual source point which results in a higher electric potential. This effect is apparent in the electric potential maps of Fig. 15 where the electric potential is mainly of negative amplitude for low frequencies (Figs 15c and d) that gradually becomes positive as the frequency increase (Figs 15a and b).

In addition, for high frequencies when the virtual source point is located in the water near the solid–water interface the corresponding electric potential had negative amplitude and when the source point is located inside the core near the interface the electric potential at focus time is positive. However, with decreasing input source frequency there is a change of sign from positive to negative for the scanning points located inside the core and the output seismoelectric image is predominantly of negative amplitude (Figs 15c and d). In order to investigate the cause for the change in polarity, the displacement field (U) and strain (ε_{kk}) at focus time is calculated using eqs (10) and (11) at a frequency equal to 75 and 9.375 kHz. The displacement of the solid and the bulk deformation of the skeleton can be determined by

$$\mathbf{U}(\mathbf{x}, t) = -\frac{1}{\rho\omega}\nabla p \exp(-\mathrm{i}\omega t), \tag{10}$$

$$\varepsilon_{kk} = trace\left(\bar{\bar{\varepsilon}}\right) = \nabla \cdot \mathbf{U}, \tag{11}$$

where $\bar{\bar{\varepsilon}}$ denotes the strain tensor (dimensionless components) and ω the pulsation frequency. Figs 17 and 18 display the displacement field and strain real and imaginary components for both frequencies, respectively. At high frequency the displacement is concentrated around the focus point; however, at low frequency the displacement field magnitude is higher and extended more in the water zone. This causes more fluid flow between the core–water interface, generating in turn a negative amplitude electric potential similar to the focus points located near the boundary in the water zone at high frequency

Downloaded from http://gji.oxfordjournals.org/ at Colorado School of Mines on July 1, 2015

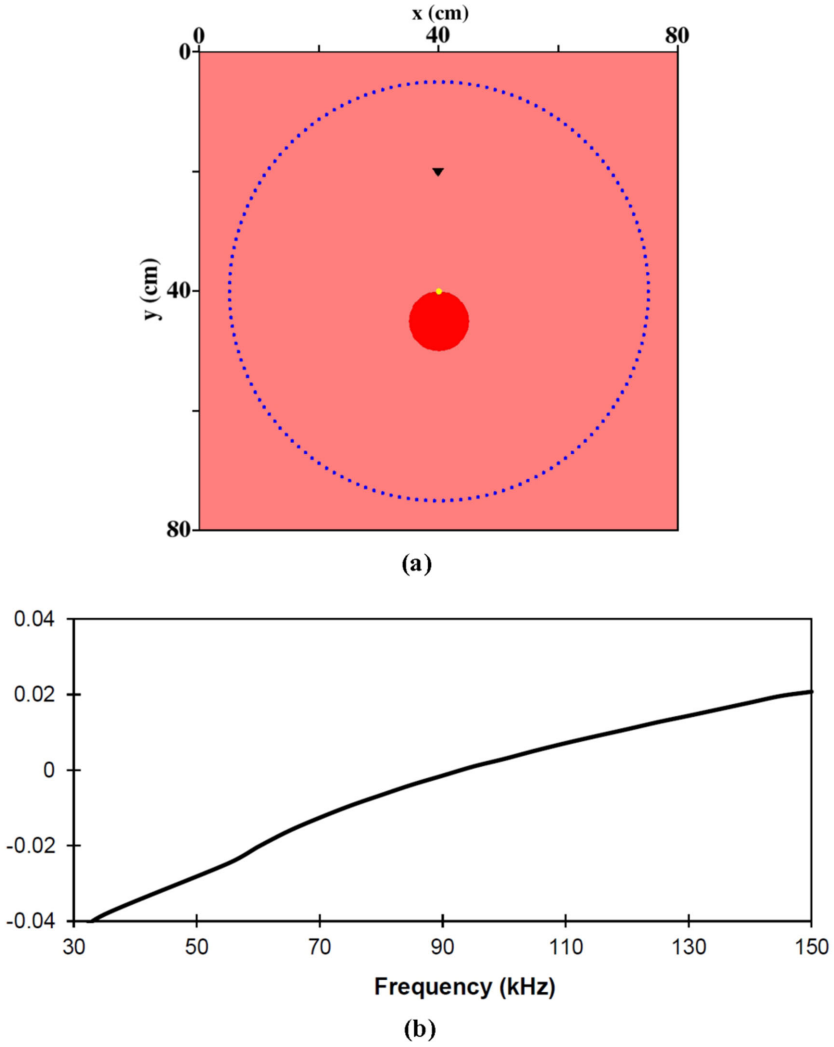

Figure 16. Electric potential versus input source frequency. (a) Schematic 2-D model of the 10 cm core centred on (45 cm, 40 cm) in the water medium with electrode E1 placed on (40 cm, 20 cm) and virtual source point (yellow point) located on (40 cm, 40 cm). (b) Normalized electric potential recorded by electrode at focus time with respect to increasing input source frequency ranging between 35 and 150 kHz while keeping all other variables constant.

(75 kHz). Similarly, the strain field shows that the entire core at low frequency is affected by the acoustic wave while at high frequency only the area near the focus point is influenced.

5 CONCLUSIONS

We investigated the resolution of the seismoelectric beamforming imaging technique within the poroacoustic approximation. This approximation is used to decrease the overall simulation time compared to a poroelastic model. However, the seismoelectric beamforming technique can be simulated using *P* waves, *S* waves or both in a porous medium and is not limited to only acoustic waves. Using exact material properties and velocity models during forward propagation of a 75 kHz dominant frequency Ricker wavelet and associated re-injection step produced a high definition and high resolution voltage map where we can recognize the location, size and shape of a cylindrical core sample in a bucket. The resolution of the seismoelectric images is highly dependent on the spacing of virtual point sources. Four scanning points per wavelength is an optimal source spacing to obtain a high definition electric potential image.

Furthermore, we analysed the sensitivity of the seismoelectric method with an incorrect velocity model. Depending on the velocity variations between the true model and estimated one, the seismic wave focus centre is shifted with scattered *P* waves across the entire medium. However, all the produced voltage maps predicted the shape of the core but the diameter is incorrect estimated in only one case (incorrect velocity model with larger core model). In addition, the electric potentials in the water zone increased (e.g. the rings) compared to the exact results due to scattered *P* waves at focus time from incorrect velocity model and the various reflections in the medium. Therefore, the knowledge of the velocity model is important in defining the quality of the output voltage map. The more complex and deviated the velocity model from reality is, the less likely the corresponding voltage map is trustworthy. That said, even with a wrong velocity model, the seismoelectric map might produce sufficient details to update the initial velocity model and re-iterate the analysis. It is therefore expected that the seismoelectric voltage map can be used in image guided inversion to improve

Downloaded from http://gji.oxfordjournals.org/ at Colorado School of Mines on July 1, 2015

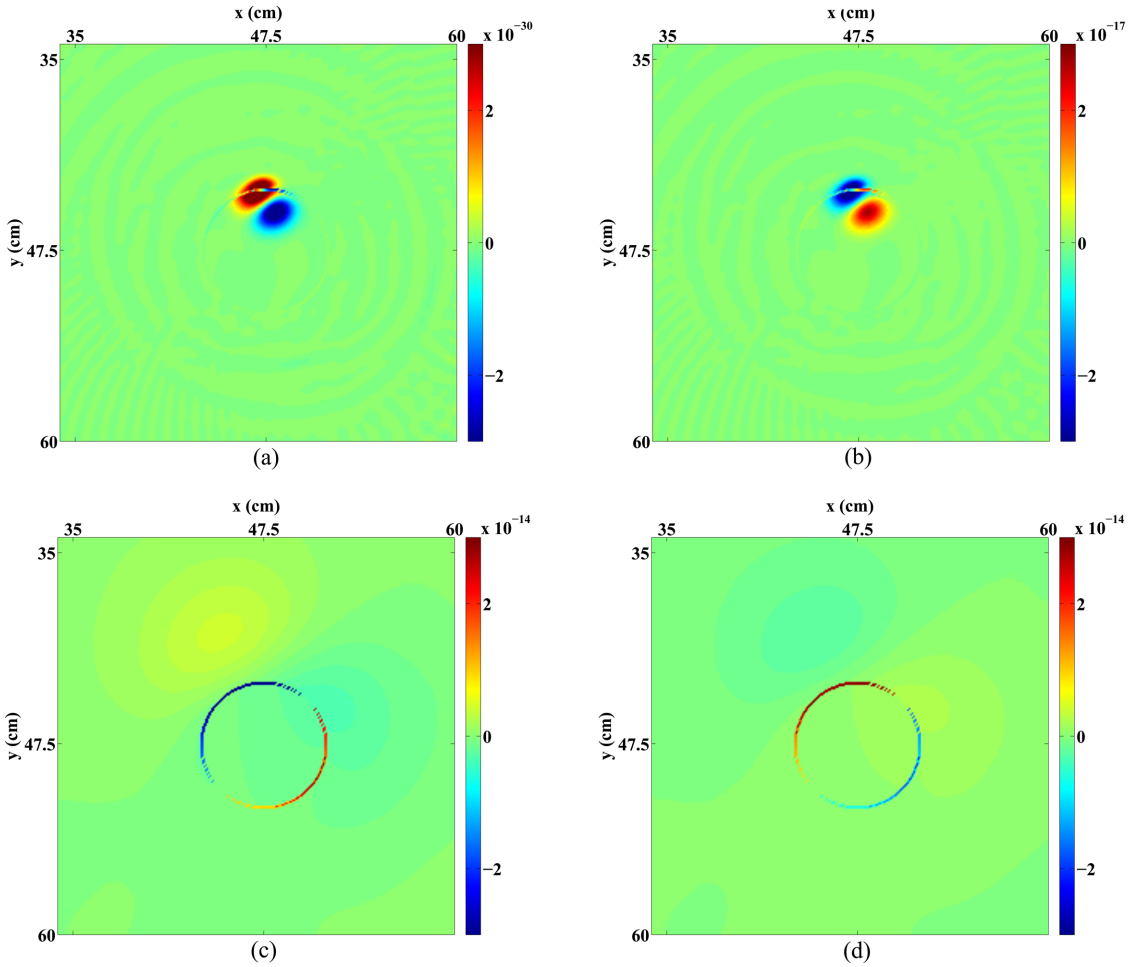

Figure 17. Displacement field at focus time for 75 and 9.375 kHz. Panels (a) and (b) represent the real and imaginary displacement field at 75 kHz, respectively. Panels (c) and (d) represent the real and imaginary displacement field at 9.375 kHz, respectively.

the velocity model itself, which may open a new way to use the seismoelectric beamforming approach.

The resolution and quality of the seismoelectric voltage map is directly related to the input source frequency with respect to the dimension of the target. As the frequency increases, the electric potential map resolution increases using at least four to eight source points per wavelength. Accordingly, to image an object, it is better to use a high-frequency source in order to obtain a detailed seismoelectric voltage map. Of course, we must always evaluate the trade-off between the quality of the image with respect to the decreasing of the magnitude of the produced voltages at high frequencies and with respect to the background noise and the attenuation of the seismic signals since Earth materials are low-pass filters. Finally, we also discussed changes in the polarity of the interface response when changing the frequency of the seismic source.

ACKNOWLEDGEMENTS

We thank Colorado School of Mines and especially Will Vaughan for funding this research though a grant to André Revil and Paul Sava. We would like to express our gratitude to Mike G. Loudin and the MENA Scholars Program at ExxonMobil Exploration Company (EMEC) for sponsoring Paul El Khoury at the Colorado School of Mines during his Master's thesis. We thank the Editor and the two referees for their time and constructive comments.

Downloaded from http://gji.oxfordjournals.org/ at Colorado School of Mines on July 1, 2015

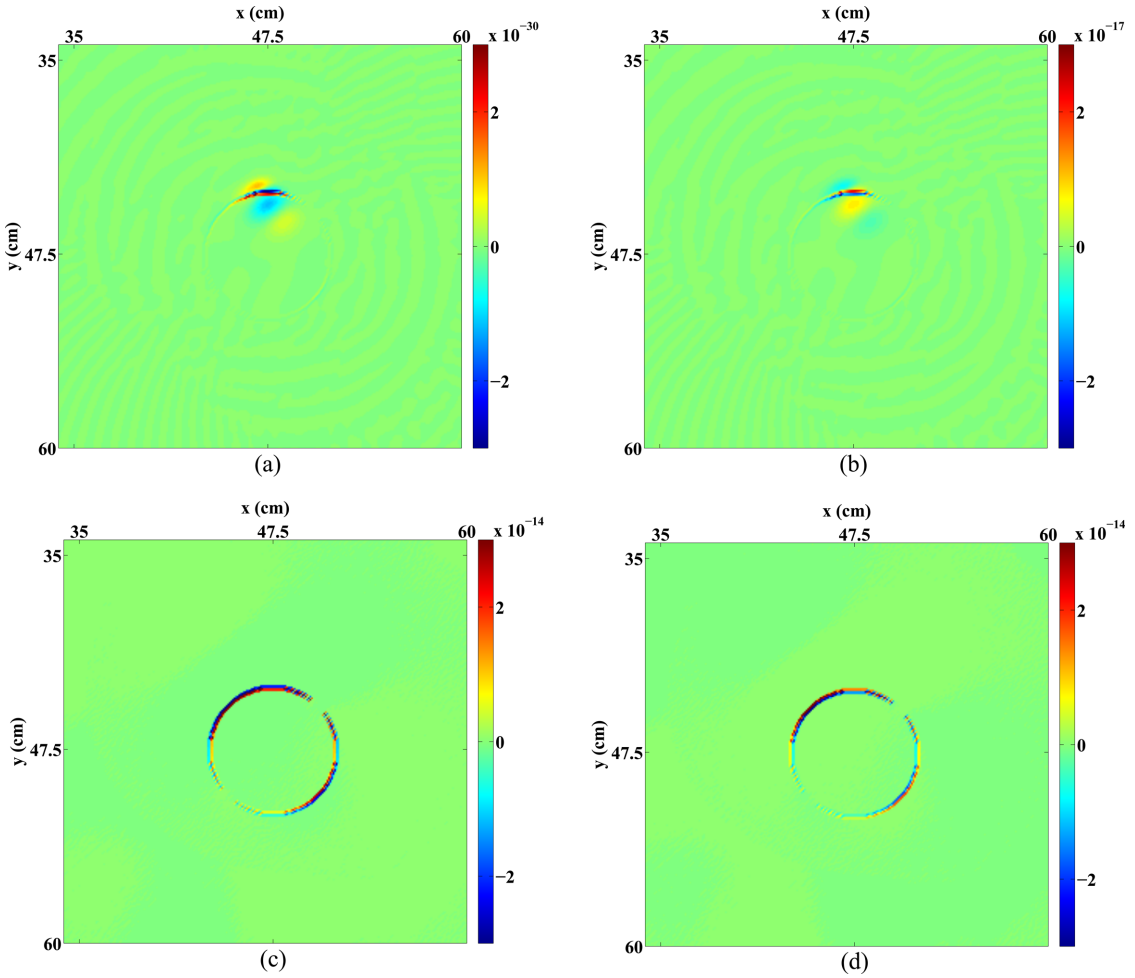

Figure 18. Distribution of the strain at focus time for 75 and 9.375 kHz. Panels (a) and (b) represent the real and imaginary strain at 75 kHz, respectively. Panels (c) and (d) represent the real and imaginary strain at 9.375 kHz, respectively.

REFERENCES

Araji, A.H., Revil, A., Jardani, A., Minsley, B.J. & Karaoulis, M., 2012. Imaging with cross-hole seismoelectric tomography, *Geophys. J. Int.,* **188,** 1285–1302.

Biot, M.A., 1962a. Generalized theory of acoustic propagation in porous dissipative media, *J. acoust. Soc. Am.,* **34,** 1254–1264.

Biot, M.A., 1962b. Mechanics of deformation and acoustic propagation in porous media, *J. appl. Geophys.,* **33,** 1482–1498.

Butler, K.E., Don Russell, R., Kepic, A. & Maxwell, M., 1996. Measurement of the seismoelectric response from a shallow boundary, *Geophysics,* **61,** 1769–1778.

Chapman, D.L., 1913. A contribution to the theory of electrocapillarity, *Philos. Mag.,* **25**(6), 475–481.

De Ridder, S.A.L., Slob, E. & Wapenaar, K., 2009. Interferometric seismoelectric Green's function representations, *Geophys. J. Int.,* **178**(3), 1289–1304.

Dupuis, J.C., Butler, K.E. & Kepic, A.W., 2007. Seismoelectric imaging of the vadose zone of a sand aquifer, *Geophysics,* **72**(6), A81–A85.

Fomel, S., Sava, P., Vlad, I., Liu, Y. & Bashkardin, V., 2013. Madagascar: open-source software project for multidimensional data analysis and reproducible computational experiments, *J. Open Res. Software,* **1,** e8.

Frenkel, J., 1944. On the theory of seismic and electroseismic phenomena in a moist soil, *J. Phys.,* **3,** 230–241.

Garambois, S. & Dietrich, M., 2002. Full waveform numerical simulations of seismoelectromagnetic wave conversions in fluid-saturated stratified porous media, *J. geophys. Res.,* **107**(B7), ESE5-1–ESE5-18.

Gouy, G., 1910. Sur la constitution de la charge électrique à la surface d'un électrolyte, *Ann. Phys. (Paris) Série,* **4**(9), 457–468.

Grobbe, N. & Slob, E., 2013. Validation of an electroseismic and seismoelectric modeling code, for layered earth models, by the explicit homogeneous space solutions, in *SEG Technical Program Expanded Abstracts,* pp. 1847–1851, Houston.

Grobbe, N., Thorbecke, J. & Slob, E., 2012. ESSEMOD—Electroseismic and seismoelectric flux-normalized modeling for horizontally layered, radially symmetric configurations, *Geophys. Res. Abstract,* **14,** 10011.

Haartsen, M.W. & Pride, S.R., 1997. Electroseismic waves from point sources in layered media, *J. geophys. Res.,* **102,** 24 745–24 769.

Haas, A.K., Revil, A., Karaoulis, M., Frash, L., Hampton, J., Gutierrez, M. & Mooney, M., 2013. Electrical potential source localization reveals a borehole leak during hydraulic fracturing, *Geophysics,* **78**(2), D93–D113.

Haines, S.S., 2004. Seismoelectric imaging of shallow targets, *Geophysics,* **77,** 9–20.

Hunter, R.J., 1981. *Zeta Potential in Colloid Science: Principles and Applications*. Academic Press.

Ivanov, A.G., 1939. Effect of electrization of earth layers by elastic waves passing through them, in *Proceedings of the USSR Academy of Sciences (Dokl. Akad. Nauk SSSR),* **Vol. 24,** pp. 42–45.

Jardani, A., Revil, A., Boleve, A., Dupont, J., Barrash, W. & Malama, B., 2007. Tomography of the Darcy velocity from self-potential measurements, *Geophys. Res. Lett.,* **34,** 1–6.

Jardani, A., Revil, A., Slob, E. & Söllner, W., 2010. Stochastic joint inversion of 2D seismic and seismoelectric signals in linear poroelastic materials: a numerical investigation, *Geophysics,* **75,** 19–31.

Downloaded from http://gji.oxfordjournals.org/ at Colorado School of Mines on July 1, 2015

Kepic, A.W., Maxwell, M. & Russell, R.D., 1995. Field trials of a seismoelectric method for detecting massive sulfides, *Geophysics,* **60,** 365–373.

Kulessa, B., Murray, T. & Rippin, D., 2006. Active seismoelectric exploration of glaciers, *Geophys. Res. Lett.,* **33,** L07503, doi:10.1029/2006GL025758.

Maxwell, J.C., 1865. A dynamical theory of the electromagnetic field, *Phil. Trans. R. Soc. Lond.,* **155,** 459–512.

Pengra, D.B., Li, S.X. & Wong, P.-Z., 1999. Determination of rock properties by low-frequency AC electrokientics, *J. geophys. Res.,* **104**(B12), 29 485–29 508.

Pride, S., 1994. Governing equations for the coupled electromagnetics and acoustics of porous media, *Phys. Rev. B,* **50,** 15 678–15 696.

Pride, S.R. & Haartsen, M.W., 1996. Electroseismic wave properties, *J. acoust. Soc. Am.,* **100,** 1301–1315.

Revil, A., 2013a. Effective conductivity and permittivity of unsaturated porous materials in the frequency range 1 mHz–1GHz, *Water Resour. Res.,* **49,** 306–327.

Revil, A., 2013b. On charge accumulations in heterogeneous porous materials under the influence of an electrical field, *Geophysics,* **78**(4), D271–D291.

Revil, A. & Jardani, A., 2010. Seismoelectric response of heavy oil reservoirs: theory and numerical modeling, *Geophys. J. Int.,* **180,** 781–797.

Revil, A. & Linde, N., 2006. Chemico-electromechanical coupling in microporous media, *J. Colloid Interface Sci.,* **302,** 682–694.

Revil, A. & Mahardika, H., 2013. Coupled hydromechanical and electromagnetic disturbances in unsaturated porous materials, *Water Resour. Res.,* **49,** 1–23.

Revil, A., Linde, N., Cerepi, A., Jougnot, D., Matthäi, S. & Finsterle, S., 2007. Electrokinetic coupling in unsaturated porous media, *J. Colloid Interface Sci.,* **313,** 315–327.

Revil, A., Mahardika, H., Barnier, G., Karaoulis, M., Sava, P., Jardani, A. & Kulessa, B., 2013. Seismoelectric coupling in unsaturated porous media: theory, petrophysics, and saturation front localization using an electroacoustic approach, *Geophys. J. Int.,* **196,** 867–884.

Revil, A., Barnier, G., Karaoulis, M., Sava, P., Jardani, A. & Kulessa, B., 2014a. Seismoelectric coupling in unsaturated porous media: theory, petrophysics, and saturation front localization using an electroacoustic approach, *Geophys. J. Int.,* **196,** 867–884.

Revil, A., Florsch, N. & Camerlynck, C., 2014b. Spectral induced polarization porosimetry, *Geophys. J. Int.,* **198,** 1016–1033.

Sava, P. & Revil, A., 2012. Virtual electrode current injection using seismic focusing and seismoelectric conversion, *Geophys. J. Int.,* **191,** 1205–1209.

Sava, P., Revil, A. & Karaoulis, M., 2014. High definition cross-well electrical resistivity imaging using seismoelectric focusing and image-guided inversion, *Geophys. J. Int.,* **198,** 880–894.

Schakel, M.D., Smeulders, D.M.J., Slob, E.C. & Heller, H.K.J., 2011. Laboratory measurements and theoretical modeling of seismoelectric interface response and coseismic wavefields, *J. appl. Phys.,* **109,** 074903, doi:10.1063/1.3567945.

Schoemaker, F.C., Grobbe, N., Schakel, M.D., de Ridder, S.A.L., Slob, E.C. & Smeulders, D.M.J., 2012. Experimental validation of the electrokinetic theory and development of seismoelectric interferometry by cross-correlation, *Int. J. Geophys.,* **514242,** 23, doi:10.1155/2012/514242.

Smeulders, D.M.J., Grobbe, N., Heller, H.K.J. & Schakel, M.D., 2014. Seismoelectric conversion for the detection of porous medium interfaces between wetting and nonwetting fluids, *Vadoze Zone J.,* **5,** 7, doi:10.2136/vzj2013.06.0106.

Warden, S., Garambois, S., Jouniaux, L., Brito, D., Sailhac, P. & Bordes, C., 2013. Seismoelectric wave propagation numerical modelling in partially saturated materials, *Geophys. J. Int.,* **194**(3), 1498–1513.

Zhu, Z., Toksöz, M.N. & Burns, D.R., 2008. Electroseismic and seismoelectric measurements of rock samples in a water tank, *Geophysics,* **73,** 153–164.

Downloaded from http://gji.oxfordjournals.org/ at Colorado School of Mines on July 1, 2015